Enigmatic crustal and upper mantle structure in the NE Sino-Korean Craton based on nuclear explosion seismic data

Xiaoqing Zhang [a,b], Hans Thybo [c,d,e,*], Irina M. Artemieva [c,d,f,g], Tao Xu [a,h], Zhiming Bai [a,h]

[a] State Key Laboratory of Lithospheric Evolution, Institute of Geology and Geophysics, Chinese Academy of Science, Beijing 100029, China
[b] University of Chinese Academy of Sciences, Beijing 100049, China
[c] SinoProbe Laboratory, Chinese Academy of Geological Sciences, Beijing, China
[d] State Key Laboratory of Geological Processes and Mineral Resources, School of Earth Science, China University of Geosciences, Wuhan, China
[e] Eurasia Institute of Earth Science, Istanbul Technical University, Maslak, 34469 Istanbul, Turkey
[f] Department of Geophysics, Stanford University, Stanford, CA 94305, USA
[g] Section of Marine Geodynamics, GEOMAR Helmholtz Center for Ocean Research, Kiel 24148, Germany
[h] Innovation Academy for Earth Science, CAS, Beijing 100029, China

ARTICLE INFO

ABSTRACT

We interpret the crustal and upper mantle structure along ~2500 km long seismic profiles in the northeastern part of the Sino-Korean Craton (SKC). The seismic data with high signal-to-noise ratio were acquired with a nuclear explosion in North Korea as source. Seismic sections show several phases including Moho reflections (PmP) and their surface multiple (PmPPmP), upper mantle refractions (P), primary reflections (PxP, PL, P410), exceptionally strong multiple reflections from the Moho (PmPPxP), and upper mantle scattering phases, which we model by ray-tracing and synthetic seismograms for a 1-D fine-scale velocity model. The observations require a thin crust (30 km) with a very low average crustal velocity (ca. 6.15 km/s) and exceptionally strong velocity contrast at the Moho discontinuity, which can be explained by a thin Moho transition zone (< 5 km thick) with strong horizontal anisotropy. We speculate that this anisotropy was induced by lower crustal flow during delamination dripping. An intra-lithospheric discontinuity (ILD) at ~75 km depth with positive velocity contrast is probably caused by the phase transformation from spinel to garnet. Delayed first arrivals followed by a long wave train of scattered phases of up to 4 s duration are observed in the 800–1300 km offset range, which are modelled by continuous stochastic velocity fluctuations in a low-velocity zone (LVZ) below the Mid-Lithospheric Discontinuity (MLD) between 120 and 190 km depth. The average velocity of this LVZ is about 8.05 km/s, which is much lower than the IASP91 standard model. This LVZ is most likely caused by rocks which are either partially molten or close to the solidus, which explains both low velocity and the heterogeneous structure.

1. Introduction

The presence of overall layering within the continental upper mantle was already proposed by Press (1961) and Hales (1969). Key global seismic discontinuities in the upper mantle include the Mid-Lithospheric Discontinuity (MLD) (Thybo and Perchuć, 1997) at about 100 km depth, the Lehmann discontinuity at approximately 210 km depth (Lehmann, 1959, 1961, 1964), and the lithosphere-asthenosphere boundary (LAB) (Artemieva, 2011) which may separate the rigid mechanical lithosphere from an underlying weak layer (asthenosphere). The exact depth, nature, and origin of these upper mantle discontinuities remain elusive, but they all have implications for our understanding of the tectonic and geodynamic evolution of the Earth.

Plate tectonics require the existence of the LAB which, however, is difficult to identify uniquely, because various methods identify different candidates for the LAB, e.g. petrologic, thermal, and seismological LAB. In seismology, the LAB is usually defined as the base of the high-velocity mantle lid at a negative velocity contrast (Eaton et al., 2009; Artemieva, 2011). It is unclear if the LAB can be identified by conversion studies, although an interface with a sharp shear velocity drop has been interpreted as the LAB (Bagley and Revenaugh, 2008; Abt et al., 2010; Rychert et al., 2010). Some interpretations of controlled source data associate the LAB with a transition from a fast seismic lid to a deeper low-velocity zone (Ryberg et al., 1996; Pavlenkova et al., 2002). The

---

depth to the LAB appears to show systematic variation between different tectonic environments, indicating that the lithosphere is generally thin (~100 km) in young tectonic regions and thick beneath stable cratons, where it usually extends to > 200 km depth (Cammarano and Roma-nowicz, 2007; Nettles and Dziewonski, 2008, Romanowicz, 2009).

The ILD is an Intra-Lithosphere Discontinuity with a positive velocity contrast, which is usually explained by spinel to garnet transformation (Hales, 1969). The MLD, at the top of a low-velocity zone, is strongly debated. A variety of evidence shows that MLD often exists beneath stable continental at a depth between ~60 km and ~160 km with a sharp velocity drop (Chen, 2009; Wittinger and Farra, 2007; Savage and Silver, 2008). In tectonically active regions, the seismic distinction be-tween the MLD and the LAB is ambiguous (Thybo, 2006; Hopper et al., 2014; Chen et al., 2014; Liu et al., 2018). Many mechanisms have been proposed to explain the origin of MLD, including variation in grain size, chemical composition, water/carbonatite content, partial melt, anisot-ropy etc. (Thybo and Perchuć, 1997; Faul and Jackson, 2005; Frost, 2006; Griffin et al., 2008; Kawakatsu et al., 2009; Dasgupta and Hirschman, 2010; Yuan and Romanowicz, 2010; Helffrich et al., 2011).

The Lehmann discontinuity is represented in the Preliminary Refer-ence Earth Model (PREM) as a discontinuity with a positive velocity contrast at a depth of ~220 km (Dziewonski & Anderson, 1981), which is usually observed as the bottom of upper mantle low-velocity zone (Thybo, 2006; Vinnik et al., 2005). Other interpretations of the Lehmann discontinuity have focused on an abrupt change in anisotropy of the mantle rocks (Montagner and Anderson, 1989; Karato, 1992; Gaherty and Jordan, 1995) or the termination of a zone of partial melting within a stable continental lithosphere (Lambert and Wyllie, 1970; Thybo and Perchuć, 1997).

There is no consensus about the upper mantle discontinuities and the interpretation of quantitative observations (e.g. depth, velocity reduc-tion, and boundary width), which are vital for analyzing these bound-aries and clarifying their origin. Active seismic methods have higher resolution than passive seismological methods. Furthermore, under-ground nuclear explosions are close to providing spherical symmetric seismic sources, which enables high-resolution identification of mantle phases (Egorkin and Chernyshov, 1983; Priestley et al., 1994; Thybo et al., 1997; Nielsen et al., 2002; Pavlenkova, 2011), and even re-flections from the core-mantle boundary can be clearly identified (Thybo et al., 2003; Ross et al., 2004).

In this paper, we interpret the upper mantle structure in the north-eastern part of the Sino-Korean Craton (SKC), which has experienced multiple subductions since the Paleozoic, and provides a unique op-portunity for studying craton activation (Xu et al., 2004b; Huang and Zhao, 2006; Zhao et al., 2009; Zheng et al., 2020; Zhu et al., 2011; Zhu and Xu, 2019; Tang et al., 2021). We interpret five profiles with length up-to 2500 km, which are recorded with a nuclear explosion as sources.

2. Seismic data

On 3 September 2017, North Korea conducted its sixth nuclear test near the China-Korea border which was registered as a seismic source with a body wave magnitude of 6.3 as reported by USGS (cf. Table 1). We have gathered three-component broadband digital seismograms based on this nuclear explosion source with 20–100 km distance be-tween stations (Fig. 1a). 291 permanent stations are from the China Earthquake Administration and the China National Digital Seismic Network (CNDSN) operated by the China Earthquake Networks Center (CENC), and 7 stations belong to portable seismic arrays in Northeast China deployed by the Institute of Geology and Geophysics, Chinese

Academy of Sciences. All seismic data were recorded with a sample rate of 10 Hz. We grouped the stations in five corridors radiating away from the source location to provide seismic sections along five profiles (Fig. 2). All five profiles show very similar features, and we will in the following interpretation concentrate on one representative profile with very dense station distribution (Fig. 1b).

Our objective is to analyze the data with a 1D upper mantle P-wave velocity model along profile 1 beneath northeastern SKC. Crustal thickness increases from ~30 km in the eastern part of the NCC to 45 km in the northwest interior of the craton (Fig. 3a) generally mirroring surface topography. This crustal thickness variation affects the trav-eltimes of observed seismic phases. We remove this effect to obtain seismic sections showing solely the effects from the upper mantle ve-locity structure by calculating static corrections to the origin time of the seismograms based on the difference in traveltime through the actual crust and a model with a constant crustal thickness of 30 km which is the mean crustal thickness of the eastern portion of the SKC (Fig. 3e). Traveltimes are calculated with the ray-tracing program RAYINVR (Zelt and Smith,1992) for the NCcrust seismic model of crustal structure (Xia et al., 2017). The processing of the digital seismic data further includes removal of the mean, and correcting to sea level datum by static change. The seismic sections are displayed with trace-normalized amplitude, a 0.1–3 Hz band-pass filter, and a reduction velocity of 8 km/s (Fig. 4).

Along the whole length of 2500 km, all sections have very high data quality and high signal-to-noise ratio, indicating very good energy propagation. The observed arrivals (Fig. 2a) can be classified into two categories.

(1) Crustal waves which include the primary reflection phases from the Moho discontinuity (**PmP**) with an apparent velocity at large offsets of ~6.2 km/s and its multiples (**PmPPmP**) with exceptionally high amplitude. The maximum offset of the observed **PmP** is 1200 km.

(2) Upper mantle waves. Clear upper mantle refractions (**P**) with an apparent velocity around 8.05 km/s are observed as first arrivals over the offset range 300–1500 km. At ~950 km offset, the first arrivals are significantly delayed in this section, which indicates the presence of a zone with reduced velocity (Thybo and Perchuć, 1997; Nielsen et al., 1999). The first arrival **P** is discontinuous and trailed by a ~5 s wave train of high-frequency scattered arrivals, primarily at offsets of 1000–1300 km. A secondary arrival (denoted as **PxP**) with apparent velocity ~8.1 km/s in the offset interval of 300–600 km is observed with very strong amplitude. Further, a high signal-to-noise phase (denoted as **PxPPmP**) is observed semi-parallel to the first arrival **P** phases within the same offset range as the **P** phases. The amplitude of the first arrival **P** and the trailing scattered coda drops significantly at ~1400 km offset, probably because the PL and P410 phases become dominant. The **PL** phase with a higher apparent velocity (8.3 km/s) is observed as the first arrival in the offset interval of 1400–1800 km as a linear phase which indicates that it is a refraction from around 200 km depth, known as the Lehmann discontinuity (Lehmann, 1961; Hales, 1991). A high-amplitude, continuous, very strong phase (**P410**) is observed at offsets of 1500–2500 km with an apparent velocity about 10 km/s, which we interpret as the reflection from the upper boundary of the mantle transition zone (the 410 km discontinuity).

3. Data modelling and results

3.1. Ray tracing forward modelling

Traveltimes of the onset of all seismic reflection/refraction phases were picked using zplot, an interactive plotting and picking software

Table 1
Event Parameters Used in This Study.

North Korean Nuclear Test	Date (yyyy/mm/dd)	Time (UTC)	Latitude (°N)	Longitude (°E)	Depth (km)	Mb (USGS)
NKT6	2017/09/03	03:30:02.23	41.303	129.070	0.640	6.3
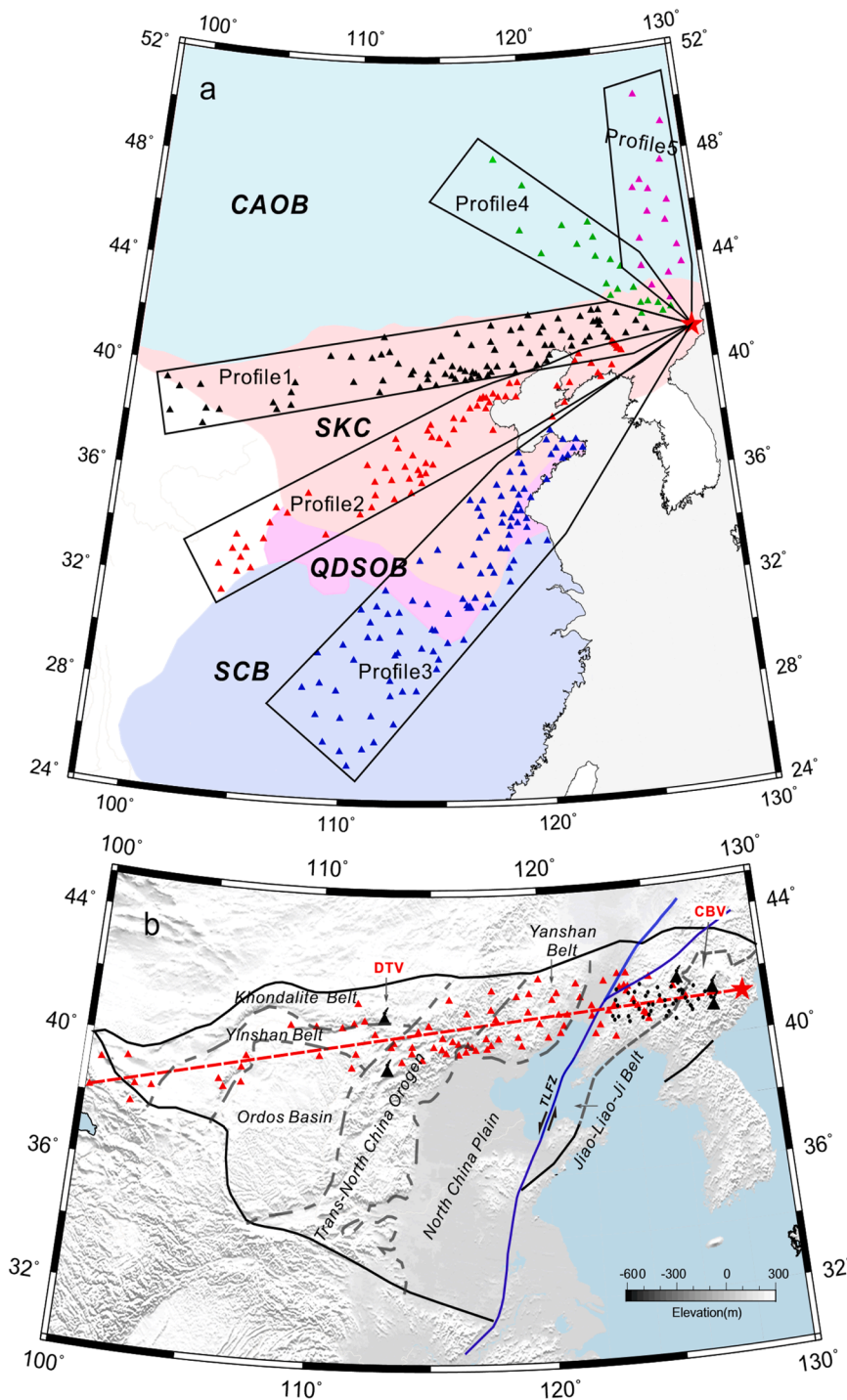
Fig. 1. (a) Map showing the location of all seismic stations and the corridors defining the five interpreted profiles. Major geological units are labeled as follows: CAOB is Central Asia Orogenic Belt; SKC is SinoKorean Craton; QDSOB is Qinling-Dabie-Sulu Orogenic Belt; SCB is South China Block. Triangles represent seismic stations. (b) Tectonic map of the Sino-Korean Craton with topography in background and location of seismic stations along profile 1. Black solid line shows the schematic cratonic edge, grey dashed line shows major tectonic boundaries, and blue line represents the Tan-Lu fault zone. Red five-point star represents the location of the sixth nuclear test conducted by North Korea. The red triangles denote seismic stations used in this study. The black points represent the reflection point of the PmP phase. Black triangles show the location of the Datong (DTV) and the Changbai (CBV) volcanoes.

package. The accuracy of the picking ranges from 100 ms to 150 ms. Notice, that only the onset of main phases were picked, also for the long codas following the main phases. The ray-tracing program RAYINVR (Zelt and Smith,1992) for two-dimensional forward modeling and inversion was used to obtain a 1D velocity model by fitting travel times of both refraction and reflection phases to constrain layer thicknesses and velocities. We use this background upper mantle structure for further detailed modelling of the observed scattered wavefield.

The calculated travel times fit the observations (Fig. 5a) with residuals of 500 ms for this simple 1D velocity model. This low residual indicates that the lateral variations in the crust and upper mantle beneath northeastern SKC are smooth.

It is an exceptional result that the average crustal velocity is 6.2 km/s for a crustal thickness of 30 km. We have checked the velocity that would result without crustal correction (Fig. S2), and find that the apparent average crustal velocity in this case would be the same, and well within the interval of 6.05–6.25 km/s. Further, ultra-long propagation of the **PmP** phase (observed out to 1200 km offset) shows that the vertical velocity gradient in the crust must be very small. The average **P** velocity of the upper mantle is about 8.05 km/s. We interpret the **PxP** phase as a primary reflection phase from an intra-lithospheric reflector at about 75 km depth. The exceptionally strong **PmPPmP** and **PxPPmP** phases must be generated at the Moho discontinuity which therefore, must be very sharp (narrow) and represent a very strong contrast in
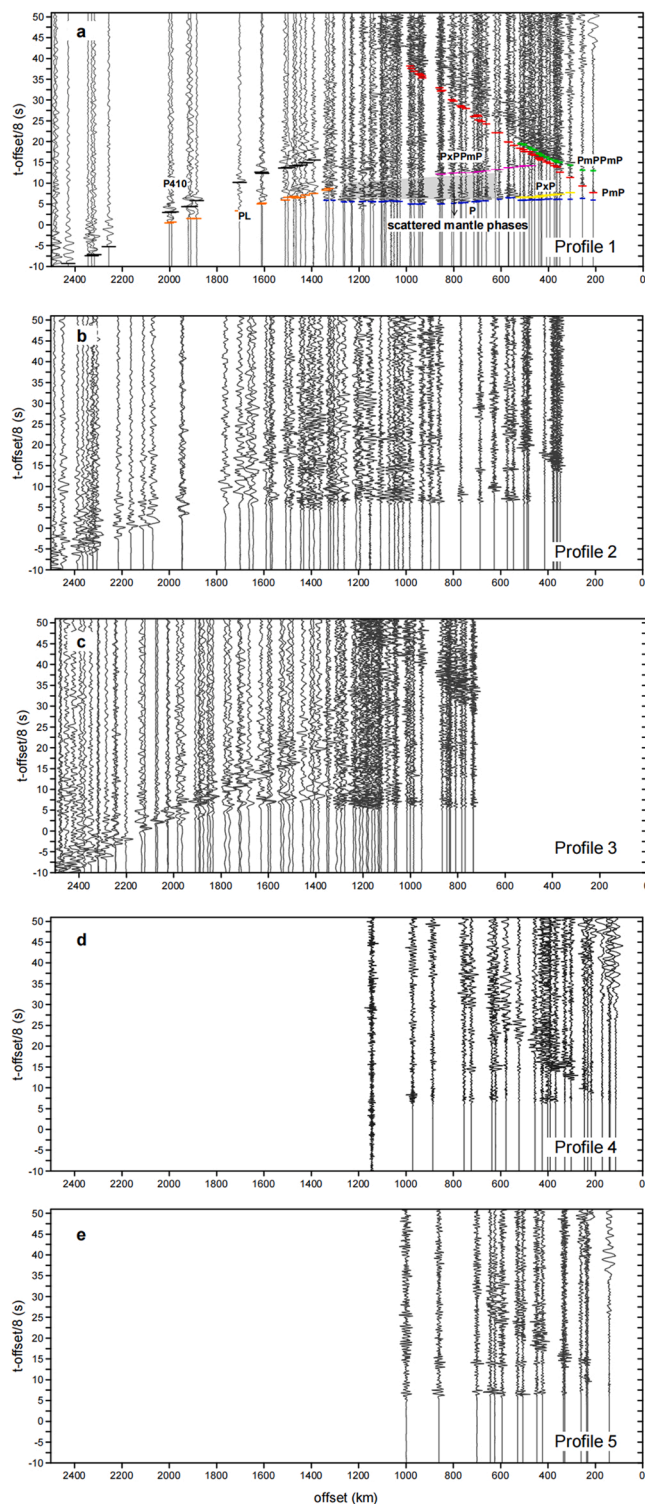
Fig. 2. Five seismic profiles were reduced by 8 km/s with station locations in Fig. 1a. The interpretation of profile 1 is illustrated in this paper. (a) Traveltime picks of seismic phases along profile1. Phase notation: PmP = reflection from the Moho; PmPPmP = surface multiple of Moho reflection; P = uppermost mantle refraction; PxP = reflection from an uppermost mantle discontinuity; PxPPmP = Moho to surface multiple of PxP; PL = reflection from the Lehmann discontinuity; P410 = reflection from the top of the mantle transition zone.

acoustic impedance at the crust-mantle boundary, as also suggested by the extremely low average crustal velocity. Delays of the P phase show the presence of a pronounced low-velocity zone below a depth of 120 km. The observed reflections and refractions from the Lehmann and the 410 km discontinuities provide further traveltime constraints on the average velocity structure in the upper mantle. The resulting model (Fig. 5d) shows that the depth to the Lehmann discontinuity is ~220 km above a layer with average velocity ~8.35 km/s and that the 410 km discontinuity is located at a depth of ~410 km above a layer with average velocity ~8.83 km/s. We emphasise that these model values are corrected for Earth's curvature.

3.2. Reflectivity modelling

The general character of the observed seismic sections indicates strong heterogeneity in parts of the upper mantle. We use the reflectivity method (Fuchs and Müller, 1971) to calculate full-waveform synthetic seismograms for 3D wave propagation in a 1D seismic velocity-depth model in order to constrain details of the upper mantle structure beneath northeastern SKC. To account for the long range of the profiles, we apply an earth-flattening transformation to depths and velocities (Biswas, 1972) (Fig. 5d) for the calculations.

3.2.1. Properties of the intra-lithospheric reflector at ~75 km depth

Traveltimes of the reflection phase (**PxP** and **PxPPmP**) constrain the depth and P-wave velocity at the top of this interface to ~75 km and 8.05 km/s, respectively. We determine the velocity contrast at this discontinuity by modelling the amplitude of the reflection by use of the general background model (Fig. 5d). We use a visual matches between the observed and synthetic waveforms as the quality criteria.

The contrast is determined by fitting the amplitude and traveltime of the calculated **PxP** and **P** phases versus offset to observation (Fig. 6). The synthetic section is regarded acceptable if it matches the following three criteria: 1) Within 500 km offset, the amplitude of the **P** phase and **PxP** phase is similar; 2) The critical offset is about 500 km at which total reflection of the **PxP** phases begins. 3) At large offset (> 750 km), the theoretical arrival time of the first arrival (the **P** phase) fits observations.

A negative velocity contrast across the interface from 8.20 km/s to 8.10 km/s (Fig. 6a) predicts too early arrival time of the **P** phase at an offset larger than 750 km. The model with a contrast of + 0.15 km/s (Fig. 6b) provides the best match between synthetic and observed waveforms and amplitudes, whereas the model with smaller contrast (from 8.05 km/s to 8.15 km/s, Fig. 6c) leads to a weak amplitude at offset with 600 km, and the model with larger contrast (from 8.05 km/s to 8.25 km/s, Fig. 6d) causes too strong amplitude of **PxP** relative to the **P** phase. We conclude that the interface represents a small positive velocity contrast from 8.05 to ~8.10 km/s. The thickness of this discontinuity cannot be determined, but the fact, that the waveforms match for a first-order discontinuity and the observed reflection has substantial amplitude, shows that it must be a sharp interface.

3.2.2. Low velocity zone in the upper mantle

The traveltime slope of the **P** first arrival in the range of 700–1300 km is about 8.05 km/s with an overall convex shape of the scattered traveltimes (Fig. 2a), which indicates that the vertical velocity gradient down to the Lehmann discontinuity must be significantly smaller than in standard Earth models, such as the IASP91 model (Kennett and Engdahl, 1991). A major feature of the first arrival **P** phase is that its amplitude is very small at offsets between ~1300 km and 1500 km (Fig. 4) which indicates that the low-velocity zone extends to the Lehmann discontinuity. It is unlikely that the **P** phase delays are caused by lateral variations in the surface velocity field because we have removed the effects of the crust on the traveltimes. Therefore, this feature should be explained by the vertical velocity structure.

A model with velocity contrast at the top boundary of this low-velocity zone (MLD – Mid-Lithospheric Discontinuity) from 8.15 km/s
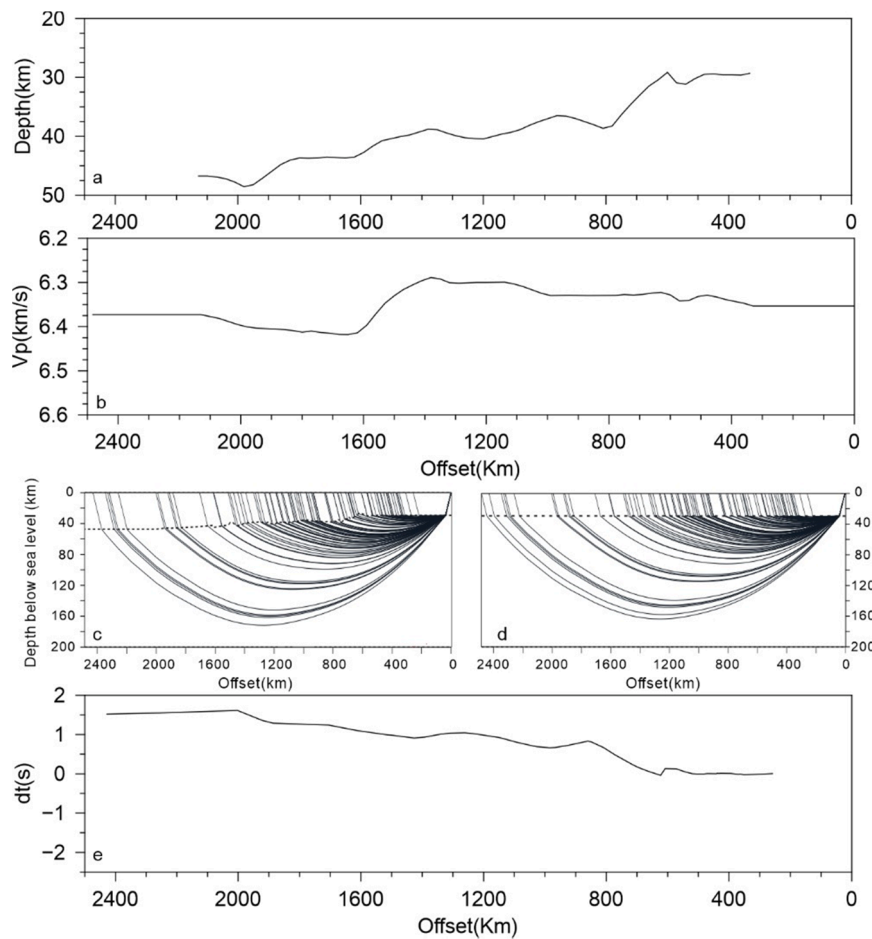
Fig. 3. Crustal thickness variation (a) and average crustal p-wave velocity (b) along profile1 as interpolated from the NCcrust model (Xia et al., 2017). Ray path of the upper mantle refraction phases calculated based on the real crustal thickness model (c) and the standard crustal model with a constant Moho depth of 30 km (d). (e) Difference in upper mantle refraction traveltime between the real crustal model and the standard crustal model.

to 8.05 km/s (Fig. 7a) predicts too early arrival time of the **P** phases at offsets larger than 1200 km, which means that the velocity gradient between **ILD** to **MLD** is smaller than this model. In observed data (Fig. 4), there is no clear reflection phase at offsets from 600 to 1200 km which means there is no pronounced velocity contrast across MLD. A model with a large velocity gradient across the Lehmann discontinuity from 8.05 km/s to 8.38 km/s (Fig. 7 b) causes a reflection phases (**PL**) with too strong amplitude, which indicate the velocity contrast at the Lehmann discontinuity is small. Model (Fig. 7e) with an average velocity about 8.05 km/s in the LVZ provides the best match between synthetic and observed waveforms and amplitudes. Meanwhile, the P phases calculated for a model with an average velocity of 8.15 km/s of LVZ (Fig. 7c) arrive too early at offsets beyond 1300 km and the LVZ with a smaller average velocity (Fig. 7d) predicts too late arrival time of the **PL** phases.

3.2.3. Seismic scattering origins from the upper mantle

Scattering phases trailing the upper mantle refraction(**P**) phase (Fig. 2a and Fig. 4) are clearly observed in our profiles. The basic observations can be summarized in three points: (1) the high-amplitude scattered phases are mainly observed at the offset range of 700–1300 km; (2) the length of the wave train of scattered arrivals decreases from approximately 13 s at ~1000 km offset to ~8 s at 1300 km offset; (3) the energy of this scattering is evenly distributed over the 8–13 s time window behind the first arrivals. Only weak scattering is observed directly behind the first arrivals at offsets < 600 km.

Seismic scattering has been observed from several depth ranges.

Lower crustal scattering is mainly observed at short offsets (<200 km) in front of the PmP reflection (e.g. Holliger and Levander, 1992), which does not match our observations. Such scattering also may cause a weak coda of scattered phases added to all mantle phases, in particular to multiply refracted Pn waves. Ryberg et al. (2000) propose a model containing horizontally thin velocity anomalies below Moho from 35 to 100 km depth, which gives rise to scattered arrivals with significant amplitude trailing the Pn. However, Nielsen and Thybo (2003) demonstrate that this mechanism does not match the observed amplitude characteristics, which can be obtained by a mechanism involving multiple scattering of the Pn phase in a highly reflective lower crust. Seismic sections calculated based on random velocity fluctuations in the upper mantle low-velocity layer (100–185 km) produce a scattered coda to the Pn from approximately 8 s at 800 km offset to around 4 s at 1400 km offset (Nielsen et al.,2002).

We explain our observed scattering by calculating synthetic seismic sections for a fluctuating medium in the low/velocity zone below MLD similar to Nielsen et al. (2002). The fluctuating medium is represented by a series of thin layers within a specific thickness (**L**) and with random velocity fluctuations in each layer following a Gaussian distribution with a standard deviation (**σ**) relative to the background model. We select L= 2–5 km and **σ** = 4 %. The seismic response is calculated by the reflectivity method (Fuchs and Müller, 1971). Based on the background model (Fig. 5d), we test three different scattering zones: (1) scatterers between the Moho and the intra-lithospheric interface (31–75 km) (Fig. 8b); (2) scatterers in the uppermost mantle between 75 and 120 km depth (Fig. 8c); (3) scatterers in the low-velocity layer (120–220 km), i.
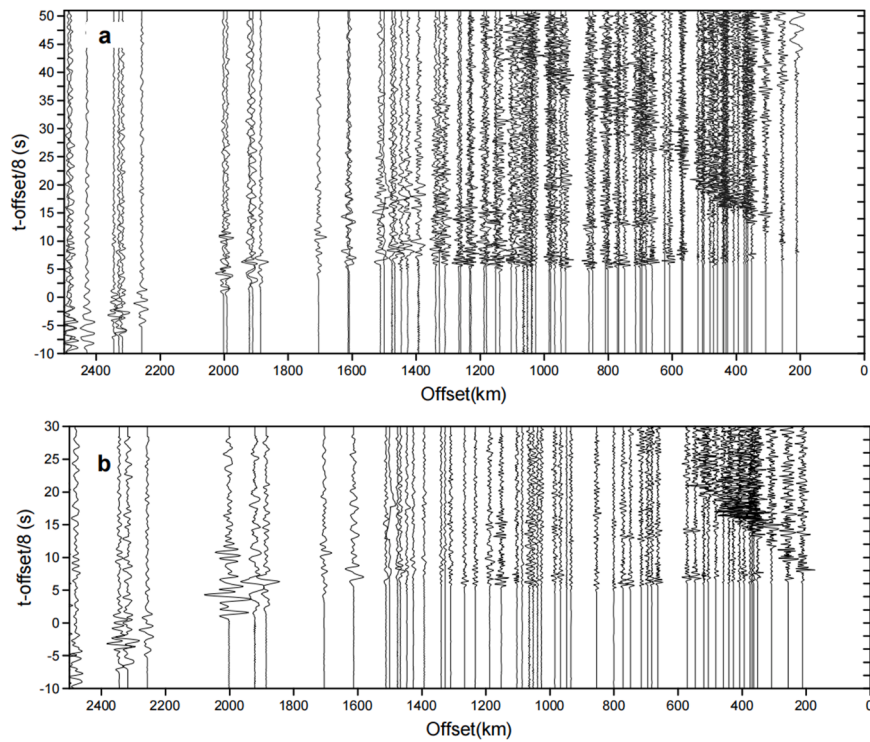
Fig. 4. Seismic section of profile 1 with a reduction velocity of 8 km/s after removing the mean, correcting the arrival delay caused by the topography and filtering with a 0.1–3 Hz band-pass filter. (a) Seismic section is displayed with trace-normalized amplitude. (b) Seismic section with true amplitude after spherical spreading compensation by the coefficient 0.000005 *x^0.8 where x is offset.
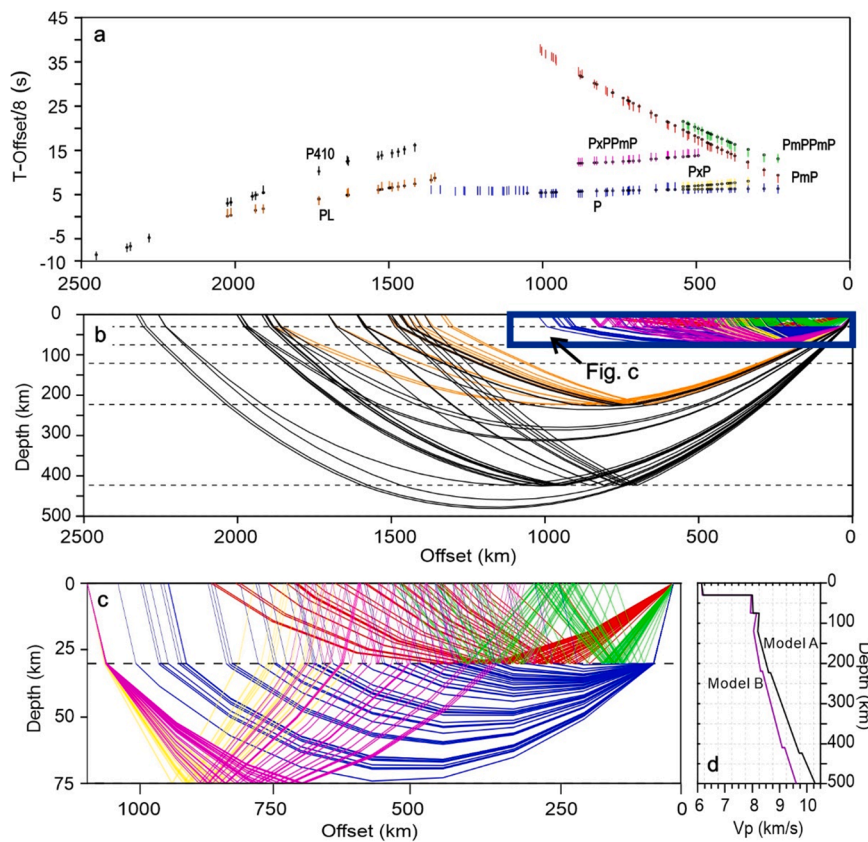
Fig. 5. (a) Traveltime fit for seismic phases used in ray-tracing interpretation of a background model. Colored bars represent the picked arrival times. Black dots represent calculated arrival time for each phase. Phase notation as in Fig. 2. (b) Ray tracing coverage of the seismic model for all modelled phases, illustrating the resolution and constrained range of this upper mantle model. Colored lines represent rays for different seismic phases. (c) zoom into the marked rectangle box in b. (d) The final obtained model A based on ray-tracing (black line) for a flat-Earth model and model B (purple line) correction for Earth-flattening in model A (velocities from the rectangular model used in RAYINVR).
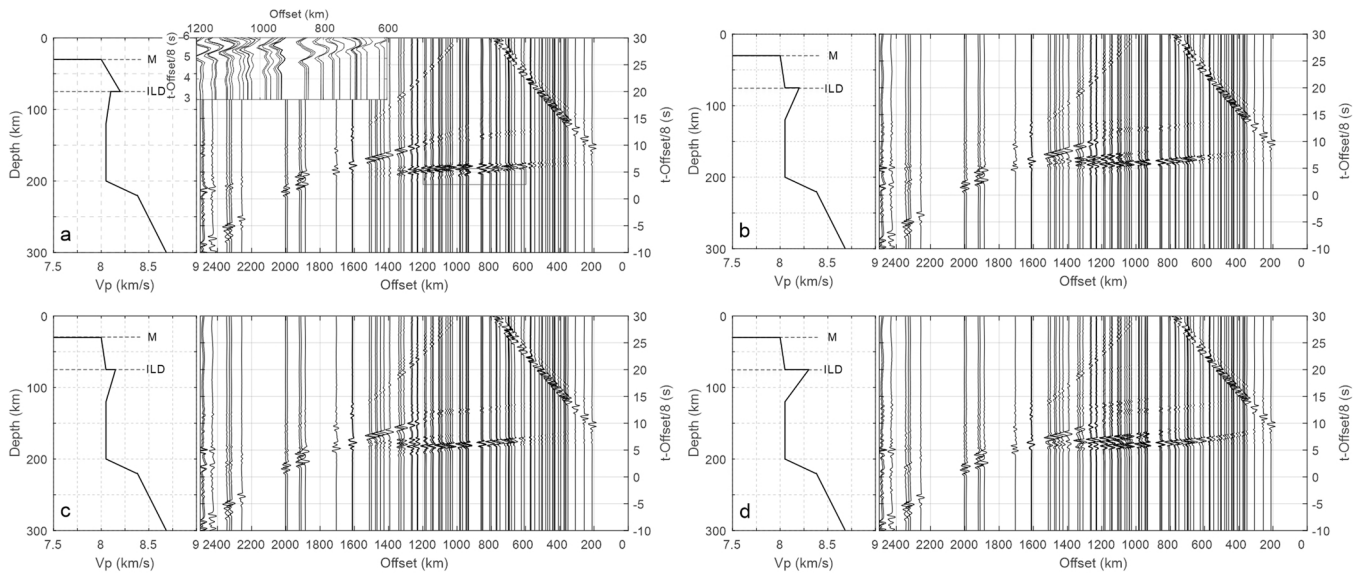
Fig. 6. Synthetic seismic sections calculated for the background model (Fig. 5d) with different velocity contrasts at ILD. All synthetic sections are shown with the same reduction velocity (8.0 km/s) and the same amplitude scaling as the observed data (Fig. 4a). A negative velocity contrast across the ILD from (a) 8.20 km/s to 8.10 km/s. A positive velocity contrast across the ILD from (b) 8.05 km/s to 8.20 km/s; (c) 8.05 km/s to 8.15 km/s; (d) 8.05 km/s to 8.25 km/s.
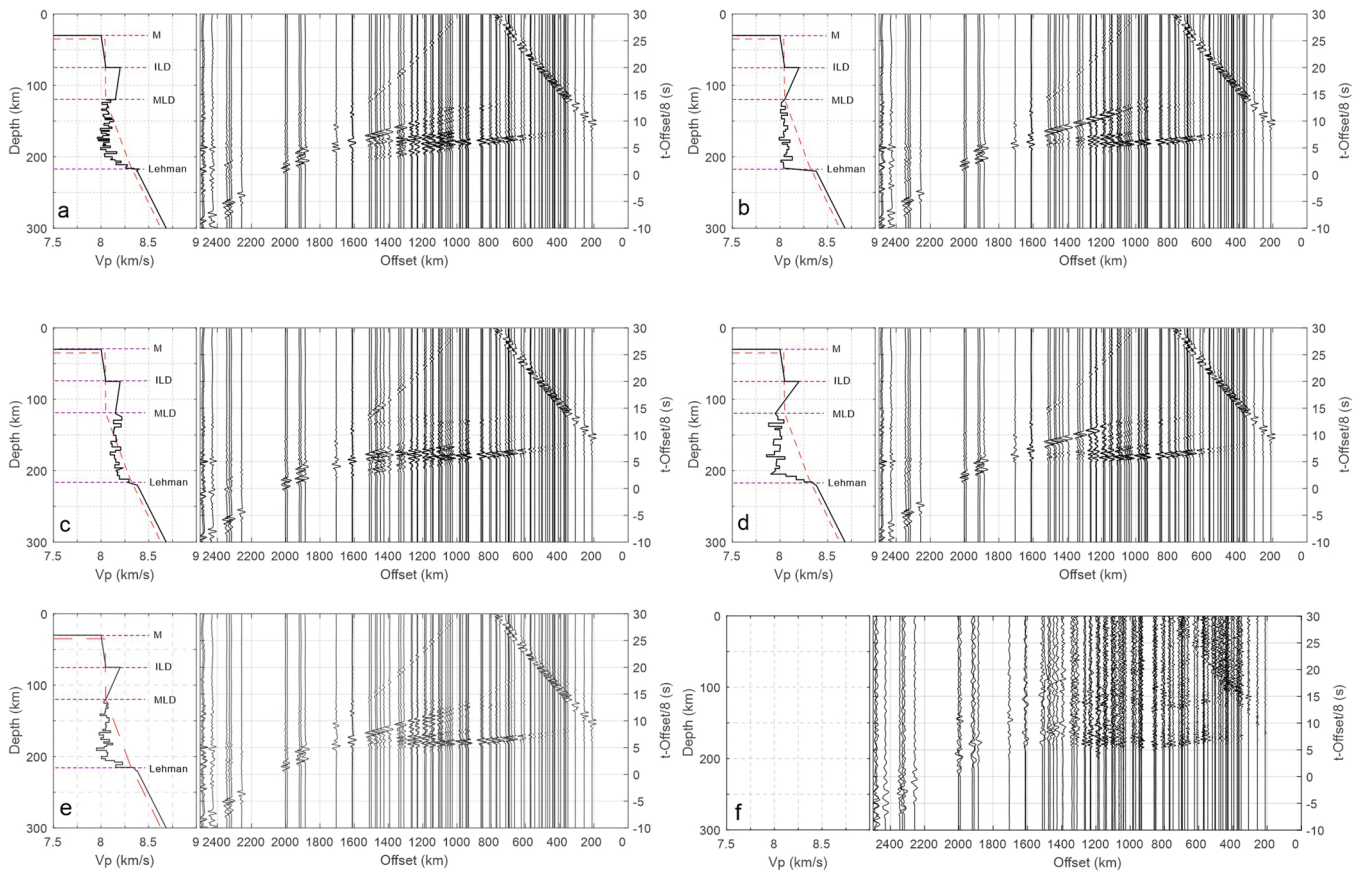
Fig. 7. Synthetic seismic sections calculated for the background model (Fig. 5d) with different structure in the LVZ. All synthetic sections are shown with the same reduction velocity (8.0 km/s) and the same amplitude scaling as the observed data (Fig. 4a). Red dashed lines represent the IASP91 model. (a) Velocity contrast across the MLD from 8.15 km/s to 8.05 km/s. (b) Velocity contrast across Lehmann discontinuity from 8.05 km/s to 8.38 km/s; (c) LVZ average velocity 8.15 km/s; (d) LVZ average velocity 7.95 km/s; (e) LVZ average velocity 8.05 km/s; (f) observed data.

e. below MLD (Fig. 8d);.

The background model cannot explain the observed scattering. Models with scatterers solely above the ILD cannot explain our

observations as they do not create sufficient coda to the P (Fig. 8b). Models with scatters from ILD to the MLD (75–120 km) doe not provide a satisfactory fit to observations because the section includes scattered
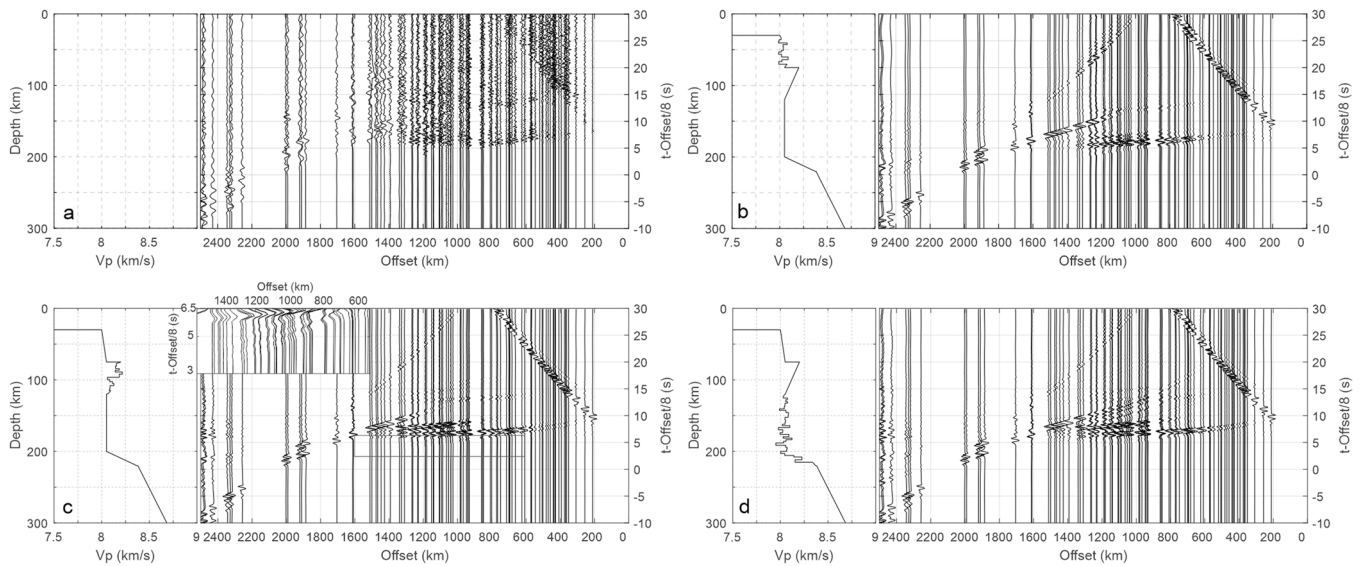
Fig. 8. Synthetic seismic sections calculated for the background model (Fig. 5d) with different scattering depth intervals. All synthetic sections are shown with the same reduction velocity (8.0 km/s) and the same amplitude scaling as the observed data (Fig. 4a). Original data (a). Synthetic sections calculated with added velocity fluctuations (b) between the Moho and the ILD; (c) between the ILD and the MLD; (d) within the LVZ.

phases earlier than the Pn at offsets between 700 and 1200 km (Fig. 8c). The synthetic section (Fig. 8d) for fluctuations in the low-velocity zone leads to scattering similar to observation (Fig. 8a). Therefore, our preferred model for the mantle beneath the northeastern SKC includes strong heterogeneity in the upper-mantle low-velocity zone.

We test the parameter space of L and σ in the ranges of 1–10 km and 2–6 % (1 % steps) for the same P-wave Q value of 500 in all tested models. We find that models with L and **σ** in the ranges of 2–5 km and 4 % generally reproduce the observed scattering (Fig. 9), as the coda extends from the Pn to the reflection phases from the deep upper mantle
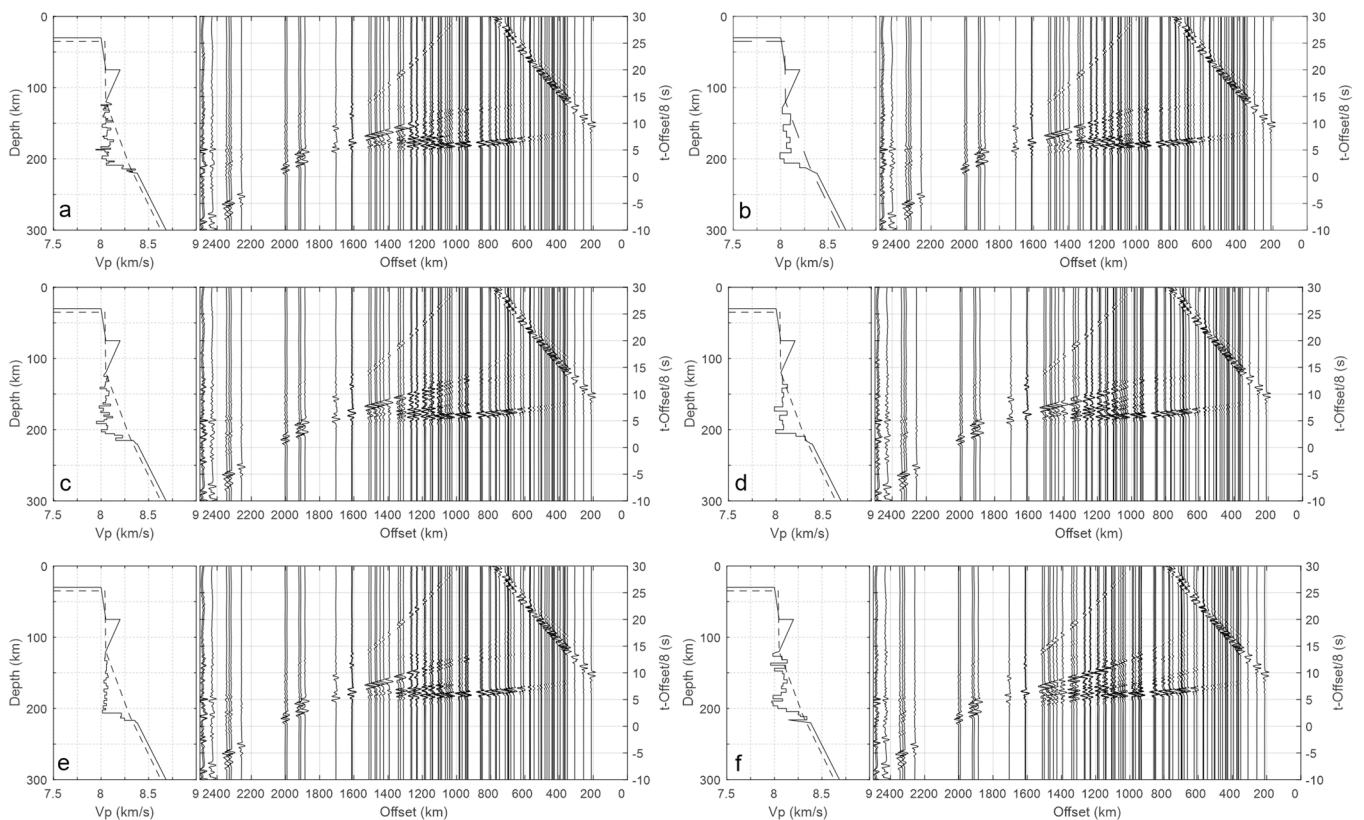
Fig. 9. Example synthetic sections with different scattering parameters (layer thickness L and standard deviation for the velocity fluctuations) in the LVZ. The Q value in the LVZ is the same (500) in all six models. All synthetic sections are shown with the same reduction velocity (8.0 km/s) and the same amplitude scaling as the observed data (Fig. 4a). Red dashed lines represent the IASP91 model. The layer thickness range of the scattering layers is following a Gaussian distribution within the intervals of 1–3 km (a), 6–9 km (b), 2–5 km (c) and 4–7 km (d), and the velocity fluctuations have constant standard deviation (4 %). The standard deviation of the velocity fluctuation is 2 % (e) and 6 % (f) for the layer thickness interval of 2–5 km as in c.

with significant amplitude. However, models with L < 2 km (Fig. 9a) lead to too weak scattering, and models with **L** > 7 km (Fig. 9b) lead to scattered phases that are too discrete at all tested velocity deviations (2 %−6 %). Model with a standard deviation of velocity fluctuation less than 3 % (Fig. 9e), leads to too weak scattering. A velocity fluctuation above the accepted 4 % (Fig. 9f) generates scattering where the amplitude is too strong at offsets less than 800 km. Therefore, we conclude that the upper mantle low-velocity zone can best be described by a series of alternating layers with thicknesses 2–7 km and a velocity fluctuation around 4 % of the background P-wave velocity (Fig. 9c, d).

We also test the effect of different P-wave attenuation values (Q) in the LVZ for our preferred values of individual layer thickness (L) and velocity. For Q values less than 300, the amplitude of the upper mantle phases is too weak (Fig. 10a1, a2), and for Q values larger than 800, the reflection from Lehmann discontinuity has too strong amplitude (Fig. 10d1, d2). Models with Q values between 500 and 800 in the LVZ fit the observations well (Fig. 10b1, b2, c1, c2).

3.3. Results

We present a 1D fine-scale crust and uppermost lithospheric mantle

structure (Fig. 11a) of the northeastern Sino-Korean Craton from a wide-angle reflection perspective using a North Korean Nuclear Explosion source profiles recorded by 80 permanent and 7 temporary broadband stations. Analysis of the crust and uppermost lithospheric mantle structure based on forward modelling and qualitative fitting shows the following:

(i) The average crustal velocity and thickness below this profile are ca. 6.17 km/s and ca 0.30 km, respectively. Ultra-long propagation of the PmP phases (to more than 1000 km offset) indicates that the vertical velocity gradient of the crust is very small, and that crustal scattering and attenuation are weak. The ray-tracing results show the crustal velocities range from 6.14 km/s in the upper crust to 6.20 km/s above the Moho discontinuity, such that the maximum vertical velocity gradient cannot be larger than 0.002 s-1.

(ii) Both the PmPPmP phases and the PxPPmP phases are multiples originating from the Moho discontinuity. The PmPPmP phase is a double reflection from the Moho discontinuity (Fig. S1a1 in the supporting information) and the PxPPmP phase is a multiple reflection from the ILD and the Moho. Both phases are
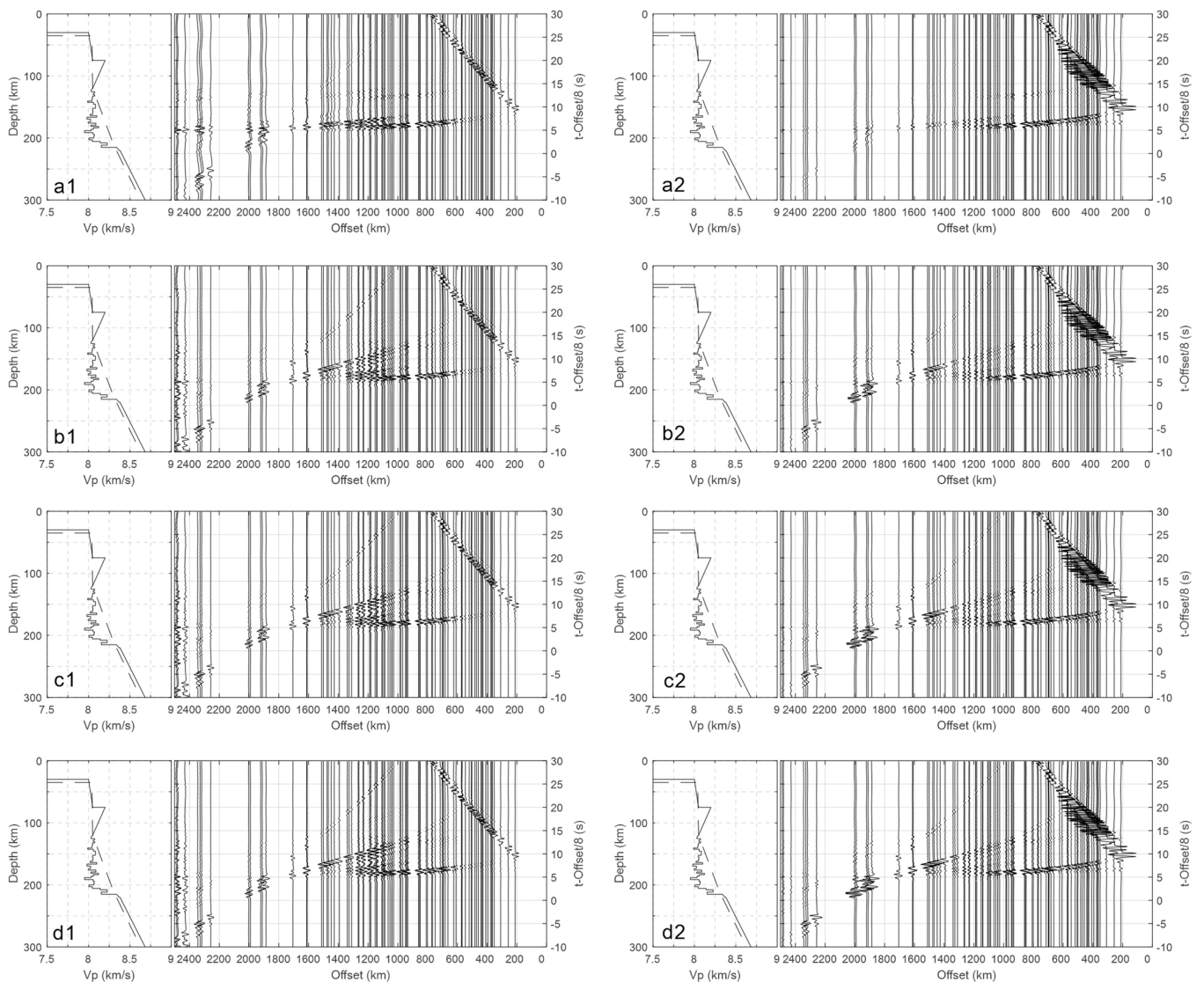
Fig. 10. Example synthetic sections with different attenuation (Q-value) in the LVZ for constant scatter layer thickness intervals and velocity distribution (4 %). All synthetic sections are shown with a reduction velocity 8 km/s. Left panels marked 1: Trace-normalized amplitude as the observed section in Fig. 4a. Right panels marked 2: Seismic sections plotted with true amplitude with spherical spreading compensation as in Fig. 4b. (a) Q= 100; (b) Q = 500; (c) Q= 800; (d) Q= 1500.
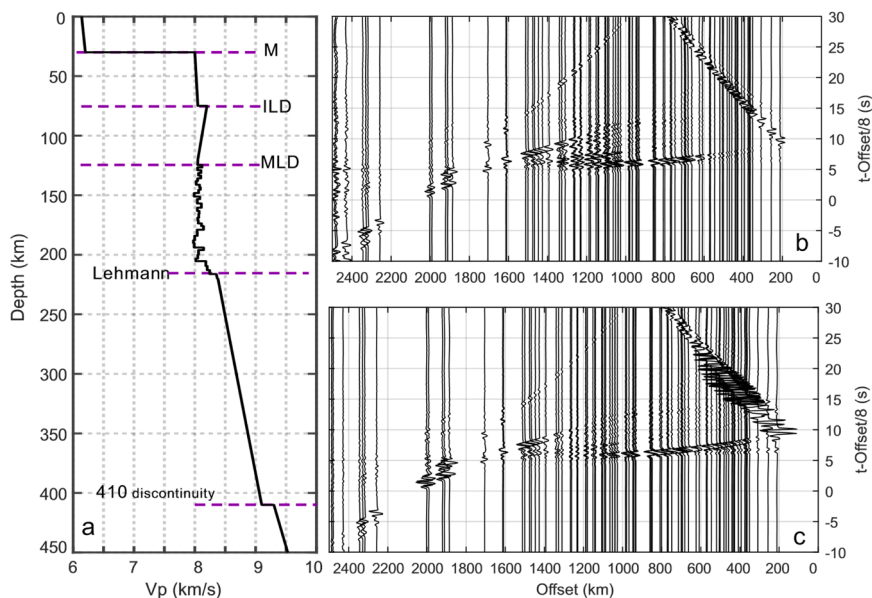
Fig. 11. Final 1D fine-scale upper mantle model beneath the northeastern SKC (a). Synthetic seismic section displayed with trace-normalized amplitude (b) and with true amplitude with spherical spreading compensation (c).

exceptionally strong for multiples, and we speculate if they may be the result of of amplitude superposition of several phases. The specific ray paths are shown in Fig. S1b3, b4, and c1 in the supporting information. The existence of the PmPPmP phase and the PxPPmP phase, both of them with extraordinary strong amplitudes, demonstrate that the velocity contrast at Moho must be extraordinarily strong.

(iii) The velocity below the Moho discontinuity is about 8.00 km/s. An intra-lithospheric interface at 75 km depth represents a positive velocity change from 8.05 km/s to about 8.20 km/s.

(iv) The low velocity zone between the MLD and the Lehmann discontinuity has an average velocity of ~8.05 km/s and a Q-value in the range from 500 to 800. There is no sharp velocity contrast at the MLD and the Lehmann discontinuity. A strong scattering coda behind Pn may be explained by inhomogeneous material within the low-velocity zone, which can be represented by a series of layers with thicknesses 2–7 km and a velocity fluctuation is 4 % of the background P-wave velocity.

4. Discussion

4.1. Upper intra-lithospheric discontinuity origin

We have identified an Intra-Lithosphere Discontinuity (ILD) at a depth of 75 km with a positive velocity contrast and a Mid Lithospheric Discontinuity (MLD or the 8° Discontinuity) with a negative velocity contrast at ca. 120 km, which represents the top of the upper mantle low-velocity zone.

ILDs and MLDs are often observed at depths around 60–160 km in stable cratons with lithosphere thicker than 200 km (e.g. Thybo and Perchuć, 1997; Jones et al., 2003; Rychert and Shearer, 2009; Yuan and Romanowicz, 2010; Rader et al., 2015; Sun et al., 2018;). The first observation was for the Baltic Shield (Perchuć and Thybo, 1996). In tectonically active regions, the Lithosphere-Asthenosphere Boundary (LAB) may occur at similar depths (60–100 km), which sometimes makes the distinction between MLD and LAB ambiguous, e.g. where a lithospheric root may have been removed, as proposed for the eastern SKC and the Wyoming Craton (Chen et al., 2014; Hopper et al., 2014). Our results include an ILD at a similar depth (85 km) in the northeastern margin of the SKC, which is consistent with results obtained by the auto correlogram method (Sun et al., 2020) and the S-wave receiver function method (Meng et al., 2021).

Until now, various mechanisms (Table 2) have been proposed to explain the origin of the MLD (and the ILD), which can be divided into thermal, compositional, and anisotropic mechanisms (Table 2 and Fig. 12):

Table 2

The possible origins of the Intra-lithosphere discontinuity and MLD.

Mechanism		Velocity variation	Depth	Reference	Acceptance
Thermal	Partial melting/fluids	Reduction	100 km ± 20 km	Thybo and Perchuć, 1997	(+)
	Partial melting/ rocks close to the solidus (80 %)	Reduction	100 km ± 20 km	Thybo, 2006	(+)
	Elastically accommodated grain-boundary sliding	Reduction	~100 km	Karato et al., 2015	(-)
Compositional	Reduction in mantle Mg# content	Reduction	Usually > 160 km	Schutt and Lesher, 2006	?
	Presence of hydrous minerals (amphibole/phlogopite)	Reduction	~3 GPa	Frost, 2006; Wyllie, 1987	(-)
	Spinel to garnet transition	Increase	2.8 ± 0.2 GPa	Robinson and Wood, 1998	(+)
	Olivine grain size variation	decrease	150 km	Faul and Jackson, 2005	(-)
Anisotropy	Changes in azimuthal anisotropy	?	?	Wirth and Long, 2014; Yuan and Romanowicz, 2010	?
	Changes in radial anisotropy	Reduction	?	Rychert and Shearer, 2009	?

(+) means an acception, (-) means an rejection and ? means an uncertain interpretation of our results.

Fig. 12. (a) The obtained 1D fine-scale upper mantle velocity model beneath the northeastern SKC. (b) Regional geotherms and solidus of peridotitic rocks. Regional geotherms are calculated based on surface heat flow data (Jiang et al., 2019) according to the methods proposed by Xia et al. (2020). C-H-O Solidus for peridotite (Wyllie et al., 1990), dry, and different bulk water contents (Katz et al., 2003) constrained by laboratory partial melting experiments.
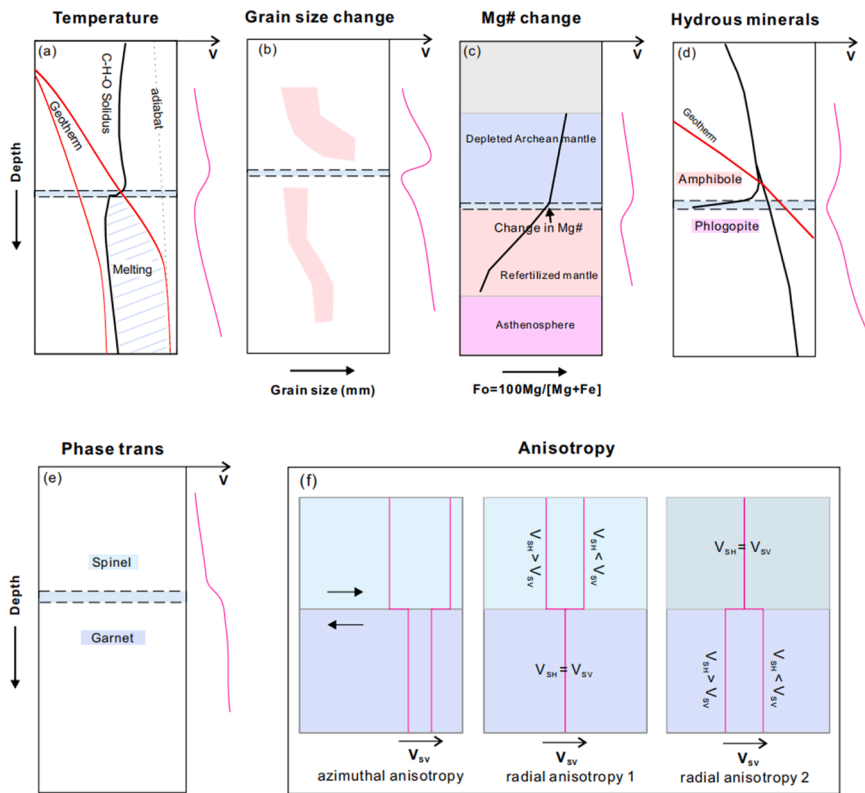
Fig. 13. Schematic diagram of possible causes of Intra-lithospheric discontinuities or MLD and corresponding velocity-depth variation. (a) Partial melting or a zone close to solidus. (b) Olivine grain-size distribution with depth for mantle peridotite xenoliths from southern African kimberlites. (c) Variation of Mg# with depth. (d) Stability field of amphibole and phlogopite. (e) Spinel to garnet transformation. (f) Layered anisotropic structure and its corresponding seismic velocity-depth variation (Karato et al., 2015).

(1) Partial melt/ fluid model (Fig. 13a). Thybo and Perchuć (1997) suggest that partial melting or fluid-related mechanisms are the most likely cause of the MLD, and Thybo (2006) proposes that the rocks in the LVZ below the MLD must be close to the solidus (within 80 %) in order to explain observations. Both mechanisms predict strong scattering from the LVZ and explain the Lehmann Discontinuity as a positive reflector at the base of the LVZ. We calculate the regional geotherms based on surface heat flow data (Jiang et al., 2019; Xia et al., 2020) and compare the depth-temperature relationships with the solidus of various upper mantle rocks, particularly the solidus of peridotites including water and carbon dioxide (Fig. 12b). The surface heat flow in our study area is 60 ± 10 mW/m^2 and, therefore, the corresponding temperature at the (upper) MLD is below or close to the solidus of carbonated peridotite. We conclude that the MLD is likely caused by the presence of partial melting.

(2) Elastically accommodated grain-boundary sliding as a thermal effect can also lead to a velocity reduction (Karato et al., 2015). With increasing temperature, seismic velocity reduction may occur because the deformation mechanism changes from elastic

to diffusional accommodation. This mechanism has a critical temperature for the transition at ~900 ± 300 ºC, which is within the calculated temperature at the ILP. However, it is debated if this mechanism can generate sufficient velocity variation to explain our observed MLD or ILD.

(3) Olivine grain-size variation. Olivine grain size distribution with depth for mantle peridotite xenoliths in cratonic upper mantle (Fig. 13b) has shown a pronounced drop in olivine grain size from ca. 4–8 mm at 120–140 km to 1 mm below 150 km. Seismic velocity decreases with olivine grain size. The strong dependence of shear modulus and attenuation on grain size allows for interpretation of the low-velocity zone in oceans by variations in grain size without requiring the presence of melts or fluids (Faul and Jackson, 2005). However, this can only explain the observations for wet mantle, The mechanism cannot explain the presence of the seismic LVZ in cratonic mantle in the absence of water or melt.

(4) Compositional changes and metasomatism are possible causes for the ILD:

(a) Decrease of mantle Mg# with depth (Fig. 13c). In the garnet stability field (>70 km depth), seismic velocities increase with increasing Mg#. Experimental data show that a 2 % velocity reduction requires a change in Mg# which is larger than 5 % (Schutt and Lesher, 2006). The composition of peridotite xenoliths (Zheng et al., 2001) from the Eastern and Central Zones of the SKC indicates that two types of spinel facies are present: high-Mg# (>=92) and low-Mg# (<91) peridotites based on Fo, which suggests that the SKC experienced significant modification after its formation. The high-Mg# peridotites are mainly refractory harzburgites, which are interpreted as relics of and old lithospheric keel, and the low-Mg# peridotites are mainly lherzolites, which are different from mantle peridotites beneath typical Archean cratons an therefore are interpreted as originating from newly accreted lithospheric mantle (Tang et al., 2008; Zhang et al., 2008). However, there is no evidence that the Mg# should show abrupt variation at the transition from lithospheric keel to newly accreted lithospheric mantle, which should generate a sharp velocity drop. Further, the velocity increases across our observed ILD. Therefore, the origin of the ILD cannot be a decrease from high-Mg# (Fo>=92) to low-Mg# (Fo <91).

(b) The presence of hydrous minerals (amphibole/phlogopite) (Fig. 13d). The seismic velocity of hydrous mantle minerals is lower than of nominally anhydrous mantle minerals. A 2–6 % velocity decrease may be explained by the presence of more than ~10 % of hydrous minerals. The maximum pressure of amphibole stability is ~3 GPa (Wyllie, 1987), whereas phlogopite has much higher maximum stability pressure and temperature (Frost, 2006). The stability depth of amphibole is close to our observed ILD depth. Xenoliths suggest that the ILD may be explained by the disappearance of amphibole in some areas, including eastern Australia and western USA, but it cannot provide a global explanation of the MLD (Selway et al., 2015). The presence of hydrous minerals has been confirmed beneath the SKC (Xu et al., 1996; Wu et al., 2017), and this mechanism, therefore, may explain our observation of the ILD.

(c) The 0.1–0.2Gpa wide spinel to garnet transition (Fig. 13e) for anhydrous fertile peridotite occurs at a pressure of 2.8 ± 0.2 GPa (Robinson and Wood, 1998), corresponding to a depth of about 85 km, which is similar to the ILD depth. Further, this phase transformation represents a velocity increase, which is consistent with our ILD observation.

(5) An abrupt change in seismic anisotropy within the mantle is a possible cause for ILD and MLD as this mechanism can produce both positive and negative velocity contrasts along our profile

(Fig. 13f). Changes in anisotropy at MLD depths have been observed in several regions including the North American Craton (Mercier et al., 2008, Yuan and Romanowicz, 2010), Central America (Wirth and Long, 2014) and the Kalahari Craton in southern Africa (Sodoudi et al.,2013). Azimuthal anisotropy is a complex and spatially variable mechanism, which can be related directly to tectonic events (Fouch and Rondenay, 2006). Although radial anisotropy may produce negative phases in SRFs (Nettles and Dziewonski,2008), studies (Wang et al.,2014) in western and northeastern SKC indicate that no continuous double-layer anisotropic structure can explain a discontinuity near both ILD and MLD depth. Amphibole shows moderately strong single crystal anisotropy (Babuska, 1991), which may lead to an anisotropic layer at a depth similar to the ILD.

4.2. Thin lower crust and strong reflection coefficient across the Moho

We constrain the average velocity and thickness of the crust below our profile to be ca. 6.17 km/s and ca. 30 km, respectively, at offsets from 100 to 500 km. This average crustal velocity is extraordinarily lower than the global average for the continental crust (Christensen and Mooney, 1995). Further, the ultra-long propagation of the Moho reflection phases beyond 1000 km, indicates that the vertical velocity gradient in the crust must be exceptionally small, and that the velocity contrast across the Moho discontinuity is extraordinarily strong (from 6.20 km/s to 8.00 km/s). The exceptionally strong multiples (PmPPmP and PxPPmPP phases) originating from the Moho discontinuity require an ultra-strong reflection coefficient at the Moho discontinuity. All evidence shows that the seismic lower crust in this area (Fig. 1b) is extremely thin (< 3 km). This observation may have two explanations:

(1) Eclogitization of the lower crust (Fig. S3b). The continental lower crust is generally inferred to be composed of 80 % mafic (53 wt % SiO2) with dominating granulite-facies rocks (Hacker et al., 2015). Compared with ultramafic rocks of the upper mantle, such mafic rocks in the lower crust have lower seismic velocities and density, which result in a significant physical properties difference between the lower crust and the upper mantle and contribute to the detectable seismic Moho, mostly interpreted as the petrological crust-mantle transition, which is marked by a sharp increase in velocity. The petrological Moho is defined by a change from felsic/intermediate/mafic crustal rocks to the dominantly ultramafic rocks of the upper mantle. However, metamorphic reactions in the lower crust and upper mantle may reduce the velocity and density contrast across the crust-mantle boundary. Granulite-facies rocks tend to transform into eclogite at large depths (>35 km), although the reaction rate and transformation conditions are debated. Eclogites usually have similar or higher seismic velocities than mantle peridotite, which makes this crust-mantle boundary hard to notable in seismology. Meanwhile, the density of the eclogite is higher than the mantle peridotite, resulting in a density inversion at the crust-mantle boundary, which may lead to lower crust delamination as proposed based on geological and geochemical arguments. However, even thick lower crustal eclogitic roots may be preserved where the delamination requirements have not been satisfied. Therefore, eclogitization of the lower crust may lead to non-coincident seismic Moho discontinuity and petrological crust-mantle boundary. In this case, the detected seismic Moho discontinuity represents the top of the eclogitic body, rather than the true crust-mantle boundary marked by a change in composition from mafic to ultramafic rocks at the bottom of the eclogitic layer. The presence of such an eclogitic lower crustal layer will result in a seismic detection of a thin crust with very low seismic velocity, as observed by our data.

All our unusual seismic observations indicate that we image the

top of an eclogitic body and not the petrological crust-mantle boundary. It appears that the "Petrological Moho" has not been imaged by the seismic data, probably because the contrast in acoustic impedance between the eclogitic body and peridotite is too small to be detected. We speculate that the base of the eclogitic layer may exist at depth of 40–50 km, similar to the depth of Moho in the central part of the NCC.

This model explains, the observed extremely low average crustal velocity and the exceptionally strong velocity contrast at the base of the small velocities. It also indicates the presence of an eclogitic layer below in our profiles. However, eclogite facies rocks have not been found at the surface, which may question the presence of eclogitic lower crust below the strong reflector. Here, we mention it as a possible, but unlikely, alternative explanation of our new observations.

(2) Strong horizontal anisotropy at the base of the thin crust (Fig. 14), which can enhance the velocity contrast (Yuan et al., 2010) at the Moho discontinuity. The evolution history of such an anisotropic thin lower crust can be roughly inferred by the following process:

The westward subduction of the paleo-western Pacific plate may have been initiated at ca. 165 Ma (Zhu et al., 2017), as constrained by age determination of accretion complexes, (Liu and Ma, 1997, Shinjiro et al., 1989, Meng et al., 2003, 2014) and analysis of structural evolution and regional sea-land distribution (Hou et al., 2015). Since ca. 60 Ma, the mid-ocean ridge between the Izanagi and Pacific plates entered the subduction zone, and the western Pacific plate began subducting after 40 Ma (Liu et al., 2017; Nohda, 2009). The continuous westward subduction of these plates caused dehydration and decompression melting in the mantle wedge (Gao et al., 2010; Zhao, 2021). Upwelling of molten mantle material and fluids led to volcanism and metasomatism, and it weakened the crust in the subduction zone (Fig. 14a). Since ca. 30 Ma (Tamaki et al., 1992), retreat and slab rollback of the western Pacific plate formed the Japan Sea as a back-arc basin with associated magmatism. Later retrieval of the subduction zone allowed the former mantle wedge to cool which intensified thermo-mechanical and chemical processes in the lower crust. The resulting formation of high-density material triggered gravitational instability and delamination. The delamination in the form of drip tectonics caused the lower crust to flow horizontally to the location of the downwelling in the weakest lithospheric mantle. Once the process was initiated, the vertical drag on the drip accelerated the horizontal flow into the drip (Fig. 14b). The combined effects of crustal extension induced by the Pacific plate retreat and horizontal flow led to thinning of the lower crust to the present thickness of only 30 km. The original thickness was probably similar to the crustal
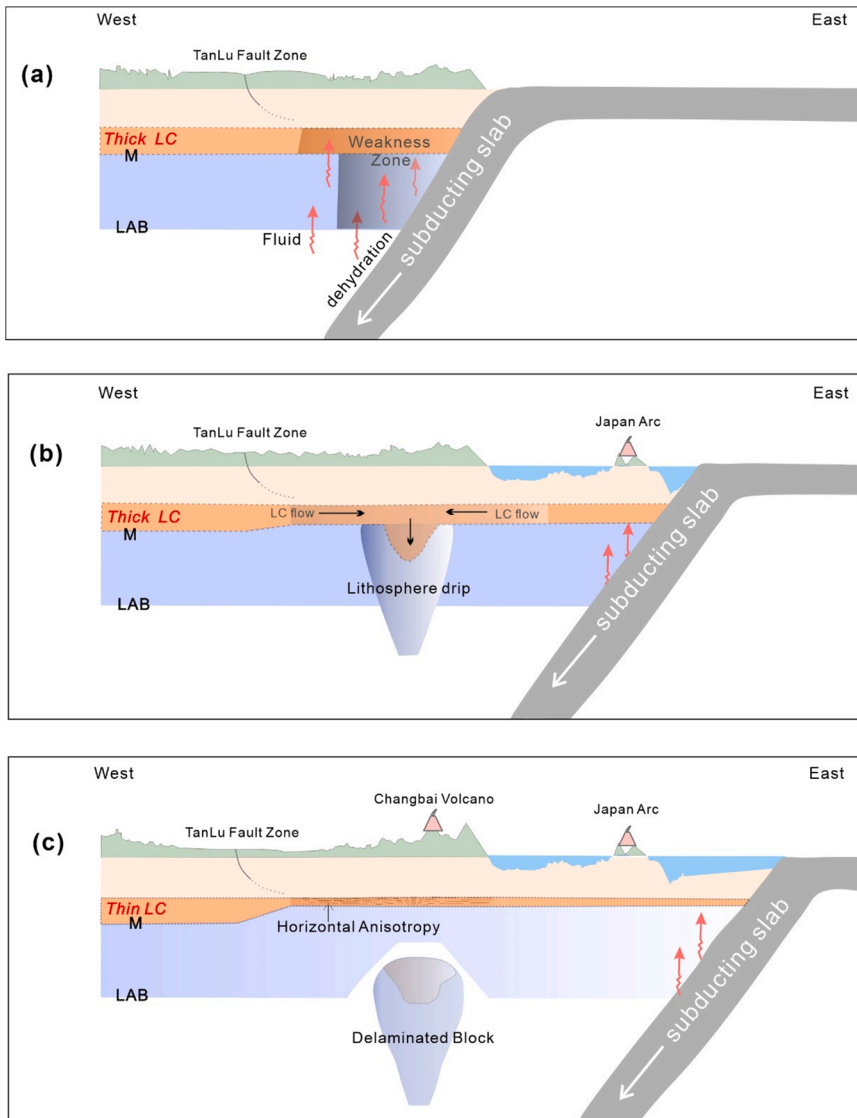
Fig. 14. Sketch of tectono-magmatic evolution of the SKC which explains our unique seismic observations of a thin crust with low average velocity and low vertical velocity gradient, as well as an extremely strong reflection coefficient at Moho beneath the northeastern SKC. (a) Early Pacific subduction creates a weak zone in the crust and mantle wedge at the magmatic arc. (b) After subduction retreat, lithospheric dripping is initiated in the weakness zone, which leads to horizontal flow in the lower crust towards the drip and causes thinning of the lower crust. (c) After delamination of the drip and cooling of the system. Crystal alignment from the lower crustal flow has caused significant anisotropy in a very thin remaining lower crustal layer. This depth interval causes extremely strong " Moho" reflections at the base of a thin crust. Abbreviations: M - Moho discontinuity. LC – Lower crust.

thickness in the SKC outside the delamination zone. The horizontal flow resulted in pronounced anisotropy in the remaining very thin lower crust, which explains the observed extremely strong reflector at the base of the crust, which from modelling results appear stronger than the very large velocity contrast from ca. 6.2–8.0 km/s suggests (Fig. 14c). The reflector strength requires anisotropy as even the observed 1.8 km/s contrast cannot reproduce the observed PmP and PmPPmp amplitudes. This model explains our unique observations of a very thin crust for a cratonic region and exceptionally strong Moho reflections.

5. Conclusions

We have presented a model for the north-eastern Sino-Korean Craton (SKC) that explains a series of unusual seismic observations in ultra-long seismic sections based on a nuclear explosion in North Korea. The model consists of a very thin crust (30 km thick) with extremely low seismic P-wave velocity (average velocity is 6.17 km/s through the whole crust) and extremely low vertical velocity gradient above an unusually strong Moho reflector. These unusual seismic properties are constrained by observations of (1) a very strong Moho reflection and (2) its very strong surface multiple which are both observed to extreme offsets of > 1000 km, as well as (3) an exceptionally strong surface-to-Moho multiple of a pronounced intra-lithospheric reflection.

We propose a model that explains the observed very thin crust and exceptionally strong Moho reflector by frozen-in anisotropy from lower crustal flow towards a lithosphere drip. The flow caused extreme thinning of the lower crust to below the seismic detection limit. We suggest that the delamination dripping took place in a zone where Pacific sub-duction had weakened the lower crust and shallow mantle before retreating to its present position. The horizontal lower crustal flow resulted in a very thin lower crust with extremely strong anisotropy caused by crystal alignment.

The high quality of the controlled source seismic sections allows for interpretation of the whole upper-mantle seismic structure after correction for the effects of crustal structure in the North China Craton. This interpretation leads to two conclusions:

First, the obtained 1-D upper mantle model (Fig. 11a) demonstrates the existence of upper mantle layering beneath northeastern SKC, which exhibits (i) an intra-lithospheric discontinuity (ILD) at a depth of 75-km with positive velocity contrast; (ii) a mid-lithosphere discontinuity (MLD) at about 120 km depth with negative velocity contrast; (iii) a prominent 70 km thick low-velocity zone (LVZ) below the MLD with an average velocity about 8.05 km/s, which is much lower than in the IASP91 model; and (iv) a positive velocity contrast at the 210-km deep (Lehmann) discontinuity. We analyze possible origins of the ILD and MLD (Figs. 12, 13 and Table 2). We find that the positive velocity contrast across the ILD most likely is related to the phase transformation from spinel to garnet. The uppermost mantle LVZ below 120 km depth appears to be a global feature in large parts of the continental mantle (Thybo, 2006) and we find that it may be caused by the presence of rocks with a temperature close to the wet solidus. The Lehmann discontinuity may mark the transition between rocks at near-solidus temperatures in the LVZ and fully solid mantle rocks.

Second, we demonstrate that the low-velocity zone (LVZ) is highly heterogeneous which causes scattering of the seismic wavefield, observed as a coda to the first arrivals in the 700–1300 km offset range. This heterogeneous medium may be represented by a series of layers with intermediate attenuation (Q = 500–800), with individual thicknesses of 2–7 km, and with velocity fluctuation described by a Gaussian distribution with a standard deviation of 4 % of the low velocity background model. There are many candidates proposed for producing such upper mantle scattering, including anisotropy and changes in rock composition. We find that changes in rock properties at temperatures close to the solidus may best explain the strong variation in velocity within the zone with very low average velocity.

CRediT authorship contribution statement

Xiaoqing Zhang: Visualization, Conceptualization, Data curation, Formal analysis, Investigation, Methodology, Software, Validation, Writing – original draft, Writing – review & editing. **Hans Thybo:** Conceptualization, Formal analysis, Software, Supervision, Validation, Writing – review & editing. **Irina M. Artemieva:** Conceptualization, Formal analysis, Supervision, Validation, Writing – original draft, Writing – review & editing. **Tao Xu:** Conceptualization, Data curation, Funding acquisition, Project administration, Supervision, Validation. **Zhiming Bai:** Conceptualization, Methodology, Software, Supervision, Validation.

Declaration of Competing Interest

The authors declare that they have no known competing financial interests or personal relationships that could have appeared to influence the work reported in this paper.

Data Availability

Digital data can be downloaded from https://github.com/pinkpinkpig-z/J.G-digital-data.git

Appendix A. Supporting information

Supplementary data associated with this article can be found in the online version at doi:10.1016/j.jog.2022.101957.

References

Abt, D.L., Fischer, K.M., French, S.W., Ford, H.A., Yuan, H., Romanowicz, B., 2010. North American lithospheric discontinuity structure imaged by Ps and Sp receiver functions. J. Geophys. Res. 115, B09301. https://doi.org/10.1029/2009JB006914.

Artemieva, I., 2011. The Lithosphere: An Interdisciplinary Approach. Cambridge University Press, Cambridge.

Babuska, V., 1991. Seismic anisotropy in the Earth, 10. Springer Science & BUsiness Media.

Bagley, B., Revenaugh, J., 2008. Upper mantle seismic shear discontinuities of the Pacific. J. Geophys. Res. 113, B12301. https://doi.org/10.1029/2008JB005692.

Biswas, N.N., 1972. Earth-flattening procedure for the propagation of Rayleigh wave. Pure Appl. Geophys 96, 61–74. https://doi.org/10.1007/BF00875629.

Cammarano, F., Romanowicz, B., 2007. Insights into the nature of the transition zone from physically constrained inversion of long-period seismic data. Proc. Natl. Acad. Sci. 104, 9139.

Chen, L., 2009. Lithospheric structure variations between the eastern and central North China Craton from S- and P-receiver function migration. Phys. Earth Planet. Inter. 173, 216–227.

Chen, L., Jiang, M., Yang, J., Wei, Z., Liu, C., Ling, Y., 2014. Presence of an intralithospheric discontinuity in the central and western North China Craton: implications for destruction of the craton. Geology 42, 223–226. https://doi.org/10.1130/G35010.1.

Christensen, N.I., Mooney, W.D., 1995. Seismic velocity structure and composition of the continental crust: a global view. J. Geophys. Res.: Solid Earth 100, 9761–9788.

Dasgupta, R., Hirschmann, M.M., 2010. The deep carbon cycle and melting in Earth's interior. Earth Planet. Sci. Lett. 298 (1), 1–13.

Dziewonski, A.M., Anderson, D.L., 1981. Preliminary reference earth model. Phys. Earth Planet. Inter. 25, 297–356.

Eaton, D.W., Darbyshire, F., Evans, R.L., Grütter, H., Jones, A.G., Yuan, X., 2009. The elusive lithosphere-asthenosphere boundary (LAB) beneath cratons. Lithos 109, 1–22. https://doi.org/10.1016/j.lithos.2008.05.009.

Egorkin, A., Chernyshov, N., 1983. Peculiarities of mantle waves from long-range profiles. J. Geophys. 54, 30–34.

Faul, U., Jackson, I., 2005. The seismological signature of temperature and grain size variations in the upper mantle. Earth Planet. Sci. Lett. 234, 119–134. https://doi.org/10.1016/j.epsl.2005.02.008.

Fouch, M.J., Rondenay, S., 2006. Seismic anisotropy beneath stable continental interiors. Phys. Earth Planet. Inter. 158, 292–332.

Frost, D.J., 2006. The stability of hydrous mantle phases. Rev. Mineral. Geochem. 62, 243–271.

Fuchs, K., Müller, G., 1971. Computation of synthetic seismograms with the reflectivity method and comparison with observations. Geophys. J. Int. 23, 417–433. https://doi.org/10.1111/j.1365-246X.1971.tb01834.x.

Gaherty, J.B., Jordan, T.H., 1995. Lehmann discontinuity as the base of an anisotropic layer beneath continents. Science 268, 1468–1471.

Gao, Y., Suetsugu, D., Fukao, Y., Obayashi, M., Shi, Y.T., Liu, R.F., 2010. Seismic discontinuities in the mantle transition zone and at the top of the lower mantle beneath eastern China and Korea: influence of the stagnant Pacific slab. Phys. Earth Planet. Inter. 5286, 8.

Griffin, W.L., O'Reilly, S.Y., Afonso, J.C., Begg, G.C., 2008. The composition and evolution of lithospheric mantle: a re-evaluation and its tectonic implications. J. Petrol. 50, 1185–1204. https://doi.org/10.1093/petrology/egn033.

Hacker, B.R., Kelemen, P.B., Behn, M.D., 2015. Continental lower crust. Annu. Rev. Earth Planet. Sci. 43, 167–205.

Hales, A.L., 1969. A seismic discontinuity in the lithosphere. Earth and Planetary Science Letters 7 (1), 44–46.

Hales, A.L., 1991. Upper mantle models and the thickness of the continental lithosphere. Geophys. J. Int. 105, 355–363.

Helffrich, G., Kendall, J.M., Hammond, J.O.S., Carroll, M.R., 2011. Sulfide melts and long-term low seismic wave speeds in lithospheric and asthenospheric mantle. Geophys. Res. Lett. 38, L11301. https://doi.org/10.1029/2011GL047126.

Holliger, K., Levander, A.R., 1992. A stochastic view of lower crustal fabric based on evidence from the Ivrea zone. Geophys. Res. Lett. 19, 1153–1156.

Hopper, E., Ford, H.A., Fischer, K.M., Lekic, V., Fouch, M.J., 2014. The lithosphere-asthenosphere boundary and the tectonic and magmatic history of the northwestern United States. Earth Planet. Sci. Lett. 402, 69–81.

Huang, J., Zhao, D., 2006. High-resolution mantle tomography of China and surrounding regions. J. Geophys. Res.: Solid Earth 111, B09305.

Jiang, G., Hu, S., Shi, Y., Zhang, C., Wang, Z., Hu, D., 2019. Terrestrial heat flow of continental China: Updated dataset and tectonic implications. Tectonophysics 753, 36–48. https://doi.org/10.1016/j.tecto.2019.01.006.

Jones, A.G., Lezaeta, P., Ferguson, I.J., Chave, A.D., Evans, R.L., Garcia, X., Spratt, J., 2003. The electrical structure of the Slave craton. Lithos 71, 505–527.

Karato, S.-i., 1992. On the lehmann discontinuity. Geophys. Res. Lett. 19, 2255–2258.

Karato, S.-i, Olugboji, T., Park, J., 2015. Mechanisms and geologic significance of the mid-lithosphere discontinuity in the continents. Nat. Geosci. 8, 509–514. https://doi.org/10.1038/NGEO2462.

Kawakatsu, H., Kumar, P., Takei, Y., Shinohara, M., Kanazawa, T., Araki, E., Suyehiro, K., 2009. Seismic evidence for sharp lithosphere-asthenosphere boundaries of oceanic plates. Science 324, 499–502.

Katz, R.F., Spiegelman, M., Langmuir, C.H., 2003. A new parameterization of hydrous mantle melting. Geochem. Geophys. Geosyst. 4, 1073. https://doi.org/10.1029/2002GC000433.

Kennett, B.L.N., Engdahl, E.R., 1991. Traveltimes for global earthquake location and phase identification. Geophys J. Int 105, 429–465. https://doi.org/10.1111/j.1365-246X.1991.tb06724.x.

Lambert, I.B., Wyllie, P.J., 1970. Low-velocity zone of the Earth's mantle; incipient melting caused by water. Science 169, 764–766.

Lehmann, I., 1959. Velocities of longitudinal waves in the upper part of the earth's mantle. Ann. Geophys 15, 93–113.

Lehmann, I., 1961. S and the structure of the upper mantle. Geophys. J., Lond. 4, 124–138.

Lehmann, I., 1964. On the velocity of P in the upper mantle. Bull. Seismol. Soc. Am. 54, 1097–1103.

Liu, D.L., Ma, L., 1997. Mesozoic tectonic evolution of continental margin in the east Asia. J. China Univ. Geosci. 11, 444–451.

Liu, L., Morgan, J.P., Xu, Y., Menzies, M., 2018. Craton destruction 1: cratonic keel delamination along a weak midlithospheric discontinuity layer. J. Geophys. Res.: Solid Earth 123 (10). https://doi.org/10.1029/2017JB015372, 040-010,068.

Liu, X., Zhao, D.P., Li, S.Z., Wei, W., 2017. Age of the subducting Pacific slab beneath East Asia and its geodynamic implication. Earth Planet. Sci. Lett. 464, 166–174.

Meng, F., Ai, Y., Xu, T., Chen, L., Wang, X., Li, L., 2021. Lithospheric structure beneath the boundary region of North China Craton and Xing Meng Orogenic Belt from S-receiver function analysis. Tectonophysics 818, 229067. https://doi.org/10.1016/j.tecto.2021.229067.

Meng, Q.R., Wei, H.H., Wu, G.L., Duan, L., 2014. Early Mesozoic tectonic settings of the northern North China Craton. Tectonophysics 611, 155–166.

Hou, F.H., Zhang, X.H., Li, G., Li, S.Z., Wen, Z.H., Li, R.H., 2015. From passive continental margin to active continental margin: basin recordings of Mesozoic tectonic regime transiton of the East China Sea shelf basin. Oil Geophys. Prospect. 50, 980–990.

Mercier, J.-P., Bostock, M., Audet, P., Gaherty, J., Garnero, E., Revenaugh, J., Mercier, C., 2008. The teleseismic signature of fossil subduction: northwestern Canada. J. Geophys. Res. 113. https://doi.org/10.1029/2007JB005127.

Montagner, J.-P., Anderson, D.L., 1989. Constrained mantle reference model. Phys. Earth Planet. Inter. 58, 205–227.

Nettles, M., Dziewonski, A.M., 2008. Radially anisotropic shear velocity structure of the upper mantle globally and beneath North America. J. Geophys. Res.: Solid Earth 113, B02303.

Nielsen, L., Thybo, H., Solodilov, L., 1999. Seismic tomographic inversion of Russian PNE data along profile Kraton. Geophys. Res. Lett. 26, 3413–3416.

Nielsen, L., Thybo, H., Egorkin, A.V., 2002. Implications of seismic scattering below the 8° discontinuity along PNE profile Kraton. Tectonophysics 358, 135–150.

Nielsen, L., Thybo, H., 2003. The origin of teleseismic Pn waves: Multiple crustal scattering of upper mantle whispering gallery phases. J. Geophys. Res.: Solid Earth 108.

Nohda, S., 2009. Formation of the Japan Sea basin: reassessment from Ar-Ar ages and Nd-Sr isotropic data of basement basalts of the Japan Sea and adjacent regions. J. Asian Earth Sci. 34, 559–609.

Pavlenkova, G.A., Priestley, K., Cipar, J., 2002. 2D model of the crust and uppermost mantle along rift profile, Siberian craton. Tectonophysics 355, 171–186.

Pavlenkova, N., 2011. Seismic structure of the upper mantle along the long-range PNE profiles — rheological implication. Tectonophysics 508, 85–95. https://doi.org/10.1016/j.tecto.2010.11.007.

Perchuć, E., Thybo, H., 1996. A new model of upper mantle P-wave velocity below the Baltic Shield: indication of partial melt in the 95 to 160 km depth range. Tectonophysics 253, 227–245.

Press, F., 1961. The Earth's Crust and Upper Mantle: New geophysical methods are beginning to reveal essential details about the earth's outer layers. Science 133 (3463), 1455–1463.

Priestley, K., Cipar, J., Egorkin, A., Pavlenkova, N., 1994. Upper-mantle velocity structure beneath the Siberian platform. Geophys. J. Int. 118, 369–378.

Romanowicz, B., 2009. The thickness of tectonic plates. Science 324, 474–476.

Rader, E., Emry, E., Schmerr, N., Frost, D., Cheng, C., Menard, J., Yu, C.-Q., Geist, D., 2015. Characterization and Petrological Constraints of the Midlithospheric Discontinuity. Geochem. Geophys. Geosyst. 16, 3484–3504. https://doi.org/10.1002/2015GC005943.

Robinson, J., Wood, B., 1998. The depth of the spinel to garnet transition at the peridotite solidus. Earth Planet. Sci. Lett. 164, 277–284. https://doi.org/10.1016/S0012-821X(98)00213-1.

Ross, A.R., Thybo, H., Solidilov, L.N., 2004. Reflection seismic profiles of the core-mantle boundary. J. Geophys. Res.: Solid Earth 109, 149–227.

Ryberg, T., Wenzel, F., Mechie, J., Egorkin, A., Fuchs, K., Solodilov, L., 1996. Two-dimensional velocity structure beneath northern Eurasia derived from the super long-range seismic profile Quartz. Bull. Seismol. Soc. Am. 86, 857–867.

Ryberg, T., Tittgemeyer, M., Wenzel, F., 2000. Finite difference modelling of P-wave scattering in the upper mantle. Geophys. J. Int. 141, 787–800.

Rychert, C.A., Shearer, P.M., 2009. A global view of the lithosphere-asthenosphere boundary. Science 324, 495–498.

Rychert, C.A., Shearer, P.M., Fischer, K.M., 2010. Scattered wave imaging of the lithosphere-asthenosphere boundary. Lithos 120, 173–185. https://doi.org/10.1016/j.lithos.2009.12.006.

Savage, B., Silver, P.G., 2008. Evidence for a compositional boundary within the lithospheric mantle beneath the Kalahari craton from S receiver functions. Earth Planet. Sci. Lett. 272, 600–609.

Schutt, D.L., Lesher, C.E., 2006. Effects of melt depletion on the density and seismic velocity of garnet and spinel lherzolite. J. Geophys. Res.: Solid Earth 111. https://doi.org/10.1029/2003JB002950.

Sodoudi, F., Yuan, X., Kind, R., Lebedev, S., Adam, J.M.C., Kästle, E., Tilmann, F., 2013. Seismic evidence for stratification in composition and anisotropic fabric within the thick lithosphere of Kalahari Craton. Geochem., Geophys., Geosystems 14, 5393–5412. https://doi.org/10.1002/2013GC004955.

Sun, W., Fu, L.-Y., Saygin, E., Zhao, L., 2018. Insights Into Layering in the Cratonic Lithosphere Beneath Western Australia. J. Geophys. Res.: Solid Earth 123, 1405–1418. https://doi.org/10.1002/2017JB014904.

Selway, K., Ford, H., Kelemen, P., 2015. The seismic mid-lithosphere discontinuity. Earth & Planet. Sci. Lett. 414, 45–57.

Shinjiro, M., Shao, J.A., Zhang, Q.L., 1989. The Nadanhada terrane in relation to Mesozoic tectonics on continental margins of east Asia. Acta Geol. Sin. 63, 204–216.

Sun, W., Zhao, L., Yuan, H., Fu, L.Y., 2020. Sharpness of the midlithospheric discontinuities and craton evolution in North China. e2019JB018594 J. Geophys. Res.: Solid Earth 125. https://doi.org/10.1029/2019JB018594.

Tang, Y.J., Zhang, H.F., Ying, J.F., Zhang, J., Liu, X.M., 2008. Refertilization of ancient lithospheric mantle beneath the central North China Craton: Evidence from petrology and geochemistry of peridotite xenoliths. Lithos 101, 435–452.

Tamaki, K., Suyehiro, K., Allan, J., Ingle, J.C., Pisciotto, K.A., 1992. 83. Tectonic synthesis and implications of Japan Sea ODP drilling. In: Proceedings of the Ocean Drilling Program, scientific results, 2. No. part, pp. 1333–1348.

Tang, Y.J., Ying, J.F., Zhao, Y., Xu, X., 2021. Nature and secular evolution of the lithospheric mantle beneath the North China Craton. Sci. China Earth Sci. 64, 1492–1503. https://doi.org/10.1007/s11430-020-9737-4.

Thybo, H., Nielsen, L., Perchuc, E., 2003. Seismic scattering at the top of the mantle Transition Zone. Earth Planet. Sci. Lett. 216 (3), 259–269 https://doi.org/10.1016/s0012-821x(03)00485-0.

Thybo, H., 2006. The heterogeneous upper mantle low velocity zone. Tectonophysics 416, 53–79.

Thybo, H., Perchuć, E., 1997. The seismic 8∘ discontinuity and partial melting in continental mantle. Science 275, 1626–1629.

Thybo, H., Perchuć, E., Pavlenkova, N., 1997. Two reflectors in the 400 km depth range revealed from peaceful nuclear explosion seismic sections. Upper Mantle Heterogeneities from Active and Passive Seismology, 17. Springer, pp. 97–103.

Vinnik, L.P., Foulger, G.R., Du, Z., 2005. Seismic boundaries in the mantle beneath Iceland: a new constraint on temperature. Geophys. J. Int. 160 (2), 533–538.

Wang, J., Wu, H., Zhao, D., 2014. P wave radial anisotropy tomography of the upper mantle beneath the North China Craton. Geochem. Geophys. Geosyst. 15, 2195–2210. https://doi.org/10.1002/2014GC005279.

Wirth, E.A., Long, M.D., 2014. A contrast in anisotropy across mid-lithospheric discontinuities beneath the central United States - a relic of craton formation. Geology 42, 851–854.

Wu, D., Liu, Y., Chen, C., Xu, R., Ducea, M.N., Hu, Z., Zong, K., 2017. In-situtrace element and Sr isotopic compositions of mantle xenoliths constrain two-stage metasomatism beneath the northern North China Craton. Lithos 288–289, 338–351.

Wyllie, P.J., 1987. Discussion of recent papers on carbonated peridotite, bearing on mantle metasomatism and magmatism. Earth Planet. Sci. Lett. 82, 391–397.

Wyllie, P.J., Baker, M.B., White, B.S., 1990. Experimental boundaries for the origin and evolution of carbonatites. Lithos 26, 3–19. https://doi.org/10.1016/0024-4937(90)90037-2.

Wittlinger, G., Farra, V., 2007. Converted waves reveal a thick and layered tectosphere beneath the Kalahari super-craton. Earth Planet. Sci. Lett. 254, 404–415.

Xia, B., Thybo, H., Artemieva, I.M., 2017. Seismic crustal structure of the North China Craton and surrounding area: Synthesis and analysis. J. Geophys. Res.: Solid Earth 122, 5181–5207.

Xia, B., Thybo, H., Artemieva, I.M., 2020. Lithosphere mantle density of the North China Craton. e2020JB020296 J. Geophys. Res.: Solid Earth 125. https://doi.org/10.1029/2020JB020296.

Xu, Y., Mercier, J.C.C., Lin, C., Shi, L., Menzies, M.A., Ross, J.V., Harte, B., 1996. K-rich glass-bearing wehrlite xenoliths from Yitong, Northeastern China: petrological and chemical evidence for mantle metasomatism. Contrib. Mineral. Petrol. 125, 406–420. https://doi.org/10.1007/s004100050231.

Xu, Y., Gang, X., Chung, S., Lin, Ma, J., Shi, L., 2004b. Contrasting cenozoic lithospheric evolution and architecture in the western and Eastern Sino-Korean Craton: Constraints from geochemistry of basalts and mantle xenoliths. J. Geol. 112, 593–605. https://doi.org/10.1086/422668.

Yuan, H., Romanowicz, B., 2010. Lithospheric layering in the North American craton. Nature 466, 1063–1069. https://doi.org/10.1038/nature09332.

Zelt, C.A., Smith, R.B., 1992. Seismic travel time inversion for 2-D crustal velocity structure. Geophys. J. Int. 108, 16–34.

Zhang, H.-F., Goldstein, S.L., Zhou, X.-H., Sun, M., Zheng, J.-P., Cai, Y., 2008. Evolution of subcontinental lithospheric mantle beneath eastern China: Re–Os isotopic evidence from mantle xenoliths in Paleozoic kimberlites and Mesozoic basalts. Contrib. Mineral. Petrol. 155, 271–293. https://doi.org/10.1007/s00410-007-0241-5.

Zhao, D., 2021. Seismic imaging of Northwest Pacific and East Asia: New insight into volcanism, seismogenesis and geodynamics. Earth-Sci. Rev. 214, 103507 https://doi.org/10.1016/j.earscirev.2021.103507.

Zhao, L., Allen, R.M., Zheng, T., Hung, S.-H., 2009. Reactivation of an Archean craton: Constraints from P- and S-wave tomography in North China. Geophys. Res. Lett. 36. https://doi.org/10.1029/2009GL039781.

Zheng, J., O'Reilly, S.Y., Griffin, W.L., Lu, F., Zhang, M., Pearson, N.J., 2001. Relict refractory mantle beneath the eastern North China block: significance for lithosphere evolution. Lithos 57, 43–66. https://doi.org/10.1016/S0024-4937(00)00073-6.

Zheng, J., Xia, B., Dai, H.-K., Ma, Q., 2020. Lithospheric structure and evolution of the North China Craton: An integrated study of geophysical and xenolith data. Sci. China Earth Sci. 64, 205–219. https://doi.org/10.1007/s11430-020-9682-5.

Zhu, R., Chen, L., Wu, F., Liu, J., 2011. Timing, scale and mechanism of the destruction of the North China Craton. Sci. China Earth Sci. 54, 789–797. https://doi.org/10.1007/s11430-011-4203-4.

Zhu, R.X., Zhang, H.F., Zhu, G., Meng, Q.R., Fan, H.R., Yang, J.H., Wu, F.Y., Zhang, Z.Y., Zheng, T.Y., 2017. Craton destruction and related resources. Int. J. Earth Sci. 106, 2233–2257.

Zhu, R., Xu, Y., 2019. The subduction of the west Pacific plate and the destruction of the North China Craton. Sci. China Earth Sci. 62, 1340–1350. https://doi.org/10.1007/s11430-018-9356-y.